



California Water and Environmental Modeling Forum

2016 ANNUAL MEETING PROCEEDINGS

Modeling Extremes: Drought to Flood and In-Betweens



CONTENTS

Introduction	1
Session 3. Incorporating Water Right Based Diversions into CalSim	
Early-season Rice Field Mapping using Landsat Imagery in the Sacramento Valley.....	2
Session 11. A Kaleidoscope of Modeling	
Fully Coupled 1-D Mobile Bed River Sediment Transport Model	7
Session 15. Advances in Integrated Modeling	
Developing Water Quality Objectives for Diversions to Agriculture from the San Joaquin River using Steady-state (Hoffman) and Transient (CSUID) Models	13
Session 16. Environmental Flows Modeling under Climate Extremes	
Using Machine Learning to Statistically Model Natural Flow: The Sacramento Watershed under Dry Conditions	19
Session 18. San Joaquin River Restoration Program 2D Hydraulic Modeling Applications	
Two-dimensional Water Temperature Modeling of In-channel and Hydraulically Connected Off-channel Zones in Reach 1A of the San Joaquin River	24
Session 20. Poster Session	
The Need for a Physically Based and Simple Estimation of MODFLOW’s River Conductance Parameter (CRIV).....	33
Session 25. Dealing with Drought: Data, Modeling, and Strategies	
Hydrology of the Recent California Drought and Comparison with Past Droughts	39
Hydroclimatic Characteristics of the 2012-2015 California Drought in a Historical Context..	49
Session 26. Multi-D Modeling	
Flow Distribution of Confluence (Fremont Weir, Sutter Bypass, Sacramento River and Yolo Bypass).....	55

INTRODUCTION

The CWEMF 2016 Annual Meeting was a huge success with 231 participants, 28 sessions, 99 oral presentations, a well-attended poster session, and an educational and entertaining pop-up session. CWEMF was honored to have the Delta Stewardship Council's Lead Scientist, Dr. Cliff Dahm give the keynote address.

CWEMF has posted copies of the Annual Meeting speakers' presentations and abstracts on the website for many years. In 2016, the CWEMF Steering Committee decided to produce an Annual Meeting Proceedings. Speakers were invited to voluntarily provide short papers summarizing their presentations. This inaugural Proceedings contains nine papers. The Steering Committee anticipates that the interest in developing papers for the Proceedings will increase in future years and that CWEMF's members will find the Proceedings useful.

Disclaimer

CWEMF and the Editor of the CWEMF Annual Meeting Proceedings are not responsible for statements and opinions printed in this publication. They represent the views of the individuals to whom they are credited. The papers were not edited and they were not send out for peer review.

Authors of papers in the Annual Meeting Proceedings can reuse material without permission from CWEMF or the Editor. Others require written permission from Authors and CWEMF.

Session 3. Incorporating Water Right Based Diversions into CalSim

Early-season Rice Field Mapping using Landsat Imagery in the Sacramento Valley

Liheng Zhong¹, Hongbing Yin², Erik Reyes³, Francis Chung⁴

¹California Department of Water Resources, Bay-Delta Office, 1416 9th Street, Sacramento, US, Liheng.Zhong@water.ca.gov

²The same affiliation and address as above, Hongbing.Yin@water.ca.gov

³The same affiliation and address as above, Erik.Reyes@water.ca.gov

⁴The same affiliation and address as above, Francis.Chung@water.ca.gov

Abstract

Water use by rice fields is one of the most critical components in the hydrologic model simulation of the Sacramento Valley, California. In this study, rice fields were mapped by an automated phenology-based approach using Landsat imagery at a very early stage of the growing season. The approach is advantageous for its capacity of mapping rice fields repeatedly, consistently and timely without the need to collect training data. Seasonal dynamics of Enhanced Vegetation Index (EVI) and Normalized Difference Moisture Index (NDMI) from segmented image series were employed to identify rice based on its phenological characteristics. A rice map was produced in late-June to forecast rice acreage and water use in the 2015 drought. The early-season map was validated by field survey data as well as an independent cropland map that was produced after the whole growing season. The high level of agreement suggests that it is possible to accurately map the spatial distribution of rice fields at an early stage by using knowledge on rice phenology to circumvent the difficulty of collecting training data within a short time. The forecast of water demand using the rice map was made on time for the model simulation of current-year hydrologic conditions.

Keywords

Land use, water demand, rice, remote sensing, classification, early-season mapping

1. Introduction

Rice is the most common crop as well as the largest water consumer in the Sacramento Valley (SacV). According to the continuous field survey by California Department of Water Resources (CDWR) and other land use data sources, rice occupies over 1/3 of agricultural land, ranking 1st among all crop types. Model simulation by CDWR Bay-Delta Office (BDO) suggests that applied water demand by rice in SacV is as high as ~3000 TAF/year. Because rice is a wetland crop, the water demand per unit area is larger than any other irrigated crop types. Therefore, the calculation of water demand is very sensitive to modeling parameters, among which land use is one of the most important factors.

Timely information on cropland use especially rice extent is essential for water management and planning for dry years. In 2015 drought, agricultural water demand in the Central Valley was evaluated month by month since the beginning of the year to determine water allocation. Real-time or semi-real-time estimate of water consumption by cropland provides an objective means to develop critical hydrological variables (for example, inflow to Delta) for water resource management. As far as we know there has not been any timely source of information on the extent of rice cultivation in the SacV. The

field survey by CDWR only covers a few counties every year, and resultant data are usually unavailable in the growing season because the fieldwork is time-consuming and labor-intensive. The USDA’s early survey on farmers’ motivation of plantation provides an estimate of total acreage before the growing season, but it offers no spatial distribution across hydrologic regions and water districts. The Cropland Data Layer by USDA is a remote-sensing-based raster map with detailed crop types, which is not released to public until the next calendar year (Boryan et al. 2011). Remote sensing is an efficient and effective way of identifying rice fields to meet the urgent need for timely crop mapping with limited resources. To facilitate real-time or semi-real-time water management especially in dry years, we develop a remote-sensing-based approach to promptly map rice extent in SacV.

2. Methods and Case Study

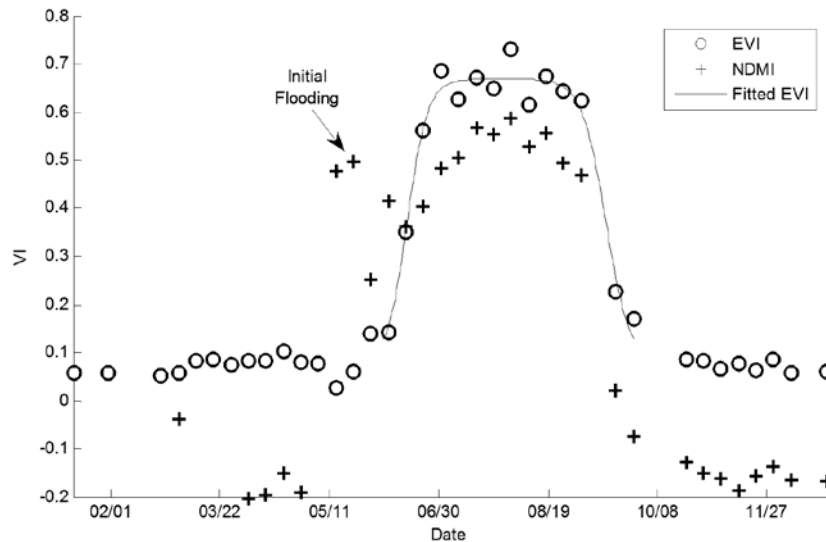
Our experiment was conducted in 8 counties on the south side of SacV: Sutter (whole), Glenn, Butte, Colusa, Yuba, Yolo, Placer, and Sacramento (partial). Most the rice cultivation in California occurs in the study area. Rice is planted in late April or May and mostly harvested in September. In the Mediterranean dry summer irrigation is the dominant source of water for rice. The entire study area falls within the Landsat scene Path 44, Row 33. Landsat 8 images at 30-meter resolution from early April to late June were used as the main input (Table 1). Cloud-covered areas on images were excluded from the analysis.

Table 1. Dates and cloud cover of Landsat 8 image series (Path 44, Row 33) for early-season mapping of rice fields.

Date acquired	Cloud cover (%)
4/6/2015	33.80
4/22/2015	3.72
5/8/2015	3.68
5/24/2015	3.07
6/9/2015	29.19
6/25/2015	0.13

Compared to dryland crops, rice is characterized by initial flooding before plantation. The unique pattern of spectral signal change around the initial flooding stage is useful in the identification of rice fields (Xiao et al. 2006; Dong et al. 2015). In this study, we used two indices derived from multi-temporal Landsat 8 images to monitor rice growth: Enhanced Vegetation Index (EVI) and Normalized Difference Moisture Index (NDMI). Both indices are calculated with a combination of Landsat 8 surface reflectance bands. EVI is capable of capturing the seasonal dynamic of vegetative vigor (Huete et al. 1997) while NDMI is sensitive to surface water content (Gao 1996). During initial flooding, NDMI is much higher than EVI, which differs from the seasonal pattern of dryland crops and natural terrestrial vegetation. Because initial flooding is finished in a short period, the increase of NDMI is very rapid, which distinguishes rice from wetlands and other inundated areas (Figure 1). Based on intensive image interpretation, time series data examination and trials with various threshold values, we found that two rules were capable of identifying rice fields in the early season: i) NDMI is larger than EVI around the initial flooding stage ($NDMI - EVI > 0$), and ii) the maximum increase rate of NDMI is greater than 0.02 per day. Figure 2b and c show the calculated images for rule implementation in an example area.

Figure 1. An example of seasonal dynamics of EVI and NDMI in rice fields.



The technique of image segmentation was employed to conduct object-based classification. Input images were segmented into relatively homogeneous polygons as minimum mapping units, which are capable of delineating cropland field boundaries and reducing the “salt and pepper” effect (Figure 2d).

3. Results and Discussion

The early-season rice map was completed in late June, right after the acquisition date of the last image in the input set (6/25/2015). By the time of completion, rice seedlings in most SacV regions had just started growing. Mapping at such an early stage is extremely challenging for traditional classification approaches that are based on vegetation signals. By utilizing the special seasonal dynamics of NDMI and EVI at initial flooding, we were able to produce a rice map that was timely for water demand forecast during 2015 drought (Figure 2a).

The rice map was validated by two independent reference datasets of 2015 cropland use: USDA CDL and CDWR land use survey data. The former is a national map covering our whole study area, and the latter is available for Butte County only. In general, the pattern of rice fields in our object-based map (Figure 2e) agrees well with the two reference datasets (Figure 2f and g). Accuracy measurements and kappa coefficient suggest that the resultant map is a reliable source of rice land use for modeling purposes (Table 2). When validated with CDWR survey data which were collected by field visits in Butte County in 2015, the user’s and the producer’s accuracies are higher than 90%. Normal rice fields and rice fields that were fallowed due to 2015 drought were both well recognized in the map.

Figure 2. (a) the study area and mapped rice extent in 2015. The small rectangle in Butte County represents the location of (b) – (g); (b) Maximum difference between NDMI and EVI; (c) Maximum daily increase rate of NDMI; (d) Polygons from image segmentation; (e) Rice extent generated from (b) – (d) and classification rules; (f) Rice fields from USDA CDL; (g) Rice fields from CDWR field survey.

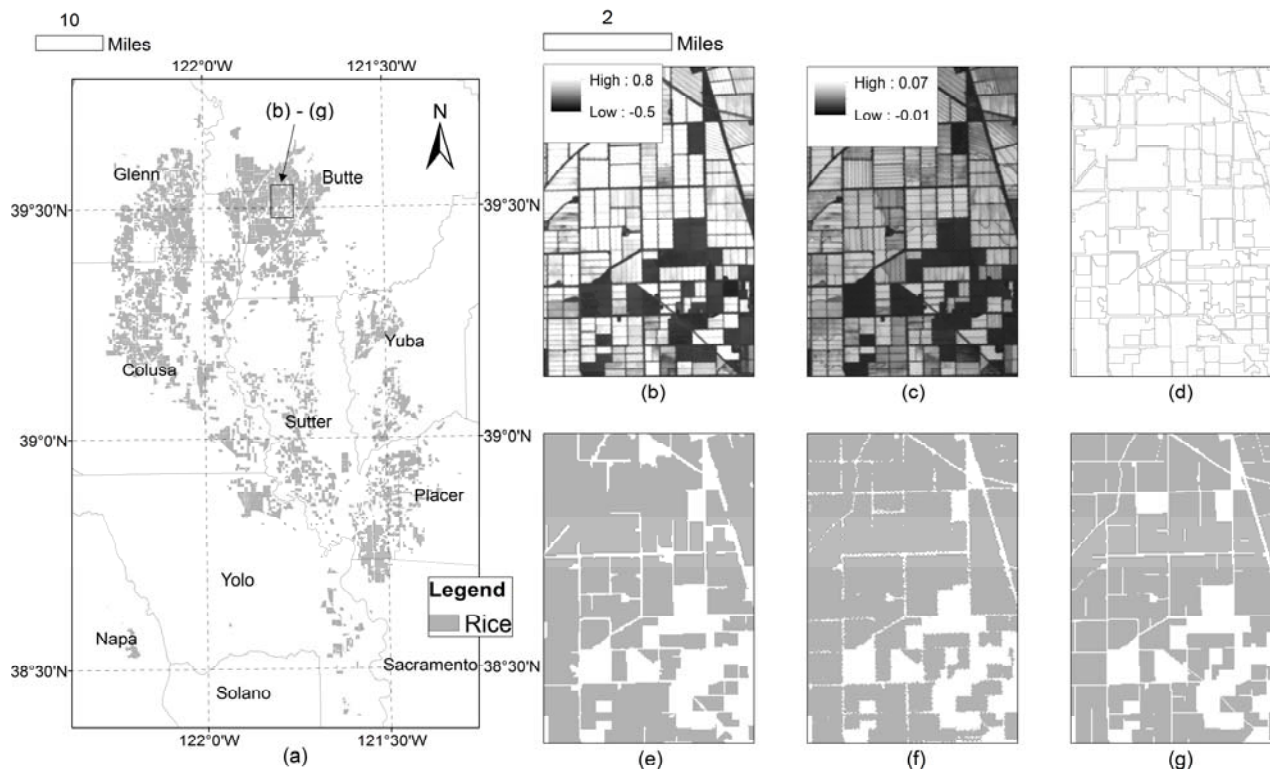


Table 2. Results of accuracy evaluation using two independent reference datasets.

Reference data	Rice classified as Rice (acre)	Other classified as Other (acre)	Rice classified as Other (acre)	Other classified as Rice (acre)	Overall accuracy (%)	User's accuracy of Rice (%)	Producer's accuracy of Rice (%)	Kappa coefficient
USDA CDL	373,955	4,174,658	62,923	26,302	98.1	93.4	85.6	0.883
CDWR Survey	78,096	625,331	6,730	5,790	98.3	93.1	92.1	0.916

4. Conclusions

In this study, we developed an efficient and effective remote-sensing-based approach to map rice fields in the Sacramento Valley. The approach is capable of producing rice maps at the beginning of the growing season year by year. Designed for repeated use at minimum cost, the mapping process does not require ground reference data. During 2015 drought, rice fields were successfully mapped in late-June, which provided timely and valuable information on the spatial distribution of rice cultivation and fallow. The combined use of techniques such as remote-sensing-based classification, time series

analysis, phenology retrieval, and image segmentation offers an excellent opportunity to perform water use estimate and hydrologic modeling based on objective, accurate, and timely land use data.

5. References

- Boryan, C., Yang, Z., Mueller, R., and Craig, M. (2011). "Monitoring US agriculture: the US Department of Agriculture, National Agricultural Statistics Service, Cropland Data Layer Program." *Geocarto Int.*, 26(5), 341-358.
- Dong, J., Xiao, X., Kou, W., Qin, Y., Zhang, G., Li, L., Jin, C., Zhou, Y., Wang, J., Biradar, C., Liu, J., and Moore III, B. (2015). "Tracking the dynamics of paddy rice planting area in 1986–2010 through time series Landsat images and phenology-based algorithms." *Remote Sens. Environ.*, 160(0), 99-113.
- Gao, B. (1996). "NDWI—A normalized difference water index for remote sensing of vegetation liquid water from space." *Remote Sens. Environ.*, 58(3), 257-266.
- Huete, A. R., Liu, H. Q., Batchily, K., and van Leeuwen, W. (1997). "A comparison of vegetation indices over a global set of TM images for EOS-MODIS." *Remote Sens. Environ.*, 59(3), 440-451.
- Xiao, X., Boles, S., Froking, S., Li, C., Babu, J. Y., Salas, W., and Moore III, B. (2006). "Mapping paddy rice agriculture in South and Southeast Asia using multi-temporal MODIS images." *Remote Sens. Environ.*, 100(1), 95-113.

Session 11. A Kaleidoscope of Modeling

Fully Coupled 1-D Mobile Bed River Sediment Transport Model (Unsteady Flow and Non-equilibrium Sediment Transport with Looped Network System)

Sungho Lee / Ph D, PE/

CVFPB (Central Valley Flood Protection Board), DWR (Department of Water Resources)
3310 El Camino Avenue, Sacramento, California 95821, USA, Sungho.Lee@water.ca.gov

Abstract

A fully coupled one-dimensional mobile bed river sediment transport model for the condition of unsteady flow and non-equilibrium sediment transport with looped network system is created to apply natural rivers. The governing equations are as follows: continuity, motion, conservation of material in suspension, conservation of bed-material, sediment transport formula and roughness equation. The above equations are solved simultaneously using the Preissmann implicit scheme. Manning roughness coefficient with the bed form (ripple and dune) considered by van Rijn method is calculated at each time step. Applying this fully coupled sediment transport model to Belley reservoir of upper Rhone River in France, total trap efficiency ($=0.4$) gives reasonably good result comparing with the measurement ($=0.49$). This model will be used to support the Basin wide and Regional flood planning study and to predict erosion of river bed, sediment deposit and trap efficiency with suspended load and bed load in channels and natural rivers.

Keywords

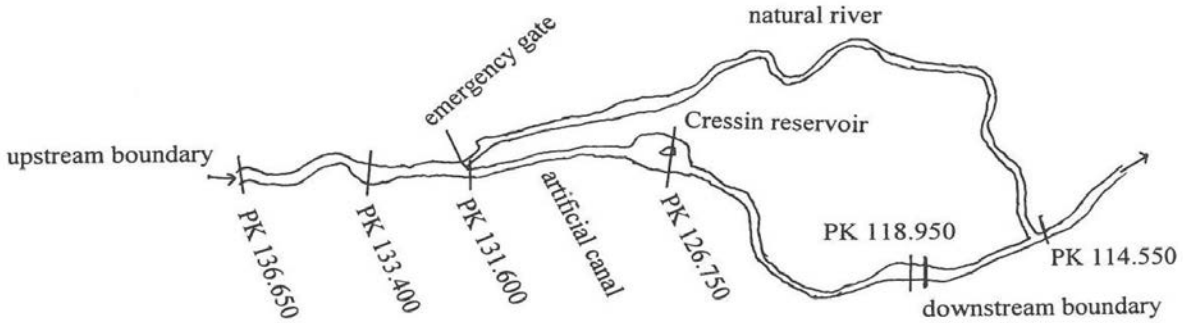
Fully coupled, one-dimensional, Mobile bed river sediment transport model, Unsteady flow, Non-equilibrium sediment transport, Bed load, Suspended load, Looped network system, Trap efficiency

1. Introduction

Belley reservoir is located at the upstream part of Rhone River in France. The flushing of Verbois reservoir and Chancy-Pougny reservoir located at the upstream of Belley reservoir is operated every 3 years to evacuate the sediment deposits in these reservoirs. Because of this flushing event, $600,000 \text{ m}^3$ of sediments are deposited at Belley reservoir after the measurement of river bed level in 1990. The length of Belley reservoir is about 18 km and the upstream reach of 4.5 km is natural river. Artificial canal with the length of 13.5 km is constructed to the downstream of hydraulic power station. (Figure 1)

The flow is divided into two parts due to island and submerged dike in Cressin reservoir. Because of the velocity difference in these two canals, the sediment transport rates are quite different. The confluence and divergence problem is included in this research because of this reason. Taking into account the interaction of stream flow, sediment transport and bed forms, the effective roughness is used to compute the Chezy or Manning roughness coefficient by the method of van Rijn. (van Rijn, 1984)

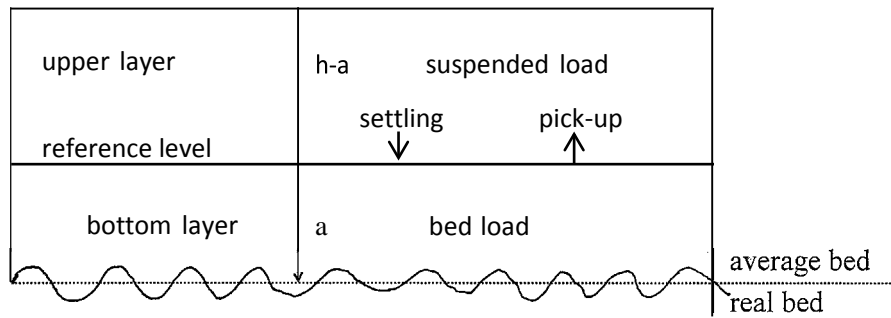
Figure 1. Map of Belley Reservoir (Upper Rhone River, France)



2. Methods and Case Study

A phenomenon considered for this model is given as follows: (Figure 2).

Figure 2. Definition Sketch in the Sediment Transport Model



2.1 Governing Equations

The one-dimensional conservation equations for the sediment transport can be described by the following primary four equations:

$$\text{Fluid continuity equation: } \frac{\partial A}{\partial t} + \frac{\partial Q}{\partial x} = B \frac{\partial z}{\partial t} + \frac{\partial Q}{\partial x} = q \quad (1)$$

$$\text{Fluid motion equation: } \frac{\partial z}{\partial t} + \frac{1}{gA} \frac{\partial}{\partial x} \left(\beta \frac{Q^2}{A} \right) + \frac{Qz}{K^2} + \frac{1}{gA} \frac{\partial Q}{\partial t} + \frac{K_e}{2g} \frac{\partial \left(\frac{Q}{A} \right)^2}{\partial x} = 0 \quad (2)$$

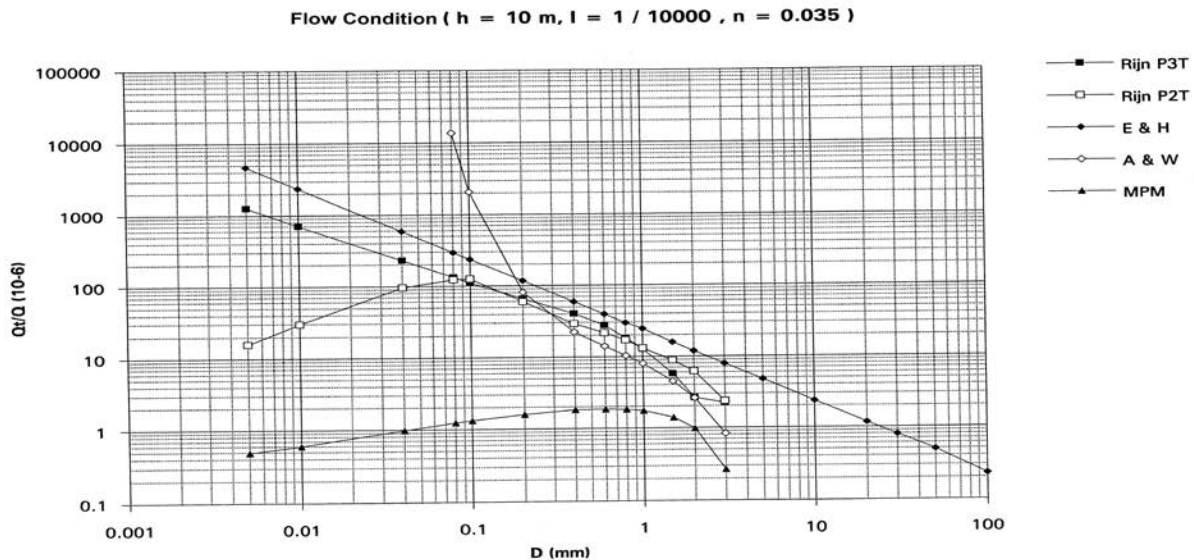
$$\text{Suspended material conservation equation: } \frac{\partial CA}{\partial t} + \frac{\partial Q_s}{\partial x} = S - qC \quad (3)$$

$$\text{Bed material conservation equation: } (1 - p) \frac{\partial A_b}{\partial t} + \frac{\partial Q_b}{\partial x} + S = 0 \quad (4)$$

in which x = streamwise coordinate; t = time; A = wetted cross-sectional area; Q = discharge; Z = water-surface elevation above a datum; B = flow width; q = lateral flow; g = gravitational acceleration; β = momentum correction coefficient; K = conveyance; K_e = coefficient of expansion-contraction; C = average sediment concentration; Q_s = volumetric suspended load; S = sediment flux between bottom layer and waterstream; A_b = bottom layer cross-section; Q_b = bed load.

To select proper sediment transport formula for natural rivers with separate suspended load and bed load condition, literature study is accomplished first. Seven sediment transport formulas are selected and tested for various hydraulic conditions: Engelund-Hansen (E &H), Ackers-White (A & W), Meyer-Peter Muller (MPM) and van Rijn' four formulas (part I – Bed Load, part II – Suspended load, Part III – Simplified Bed Load and Simplified Suspended Load) (Figure 3)

Figure 3. Example of Tested Result for Selected 7 Formulas



In addition to the above primary four governing equations, the van Rijn formula (part III, 1984) is selected and used as sediment transport formula for suspended load and bed load as follows:

$$Q_s = 0.012 \left[\frac{(V - V_{cr})}{\{(s-1)gD_{50}\}^{0.5}} \right]^{2.4} D_{50} D_*^{-0.6} V B h^{-0.2} \quad (5)$$

$$Q_b = 0.005 \left[\frac{(V - V_{cr})}{\{(s-1)gD_{50}\}^{0.5}} \right]^{2.4} D_{50}^{1.2} V B \quad (6)$$

in which s = specific density; V = mean flow velocity; V_{cr} = critical mean flow velocity based on Shield's criterion; D_{50} = median grain size of bed material; D_* = particle diameter; h = flow depth.

Roughness coefficient due to friction resistance uses Manning roughness coefficient derived from overall Chezy coefficient considering grain roughness and bed form roughness. The sediment flux between bottom layer and water stream given by Armanini and Di Silvio (1988) are applied.

In summary, a one-dimensional morphological system is described by the following seven equations:
 A. Fluid continuity equation B. Fluid motion equation C. Suspended material conservation equation
 D. Bed material conservation equation E. Sediment transport equation (Bed load and Suspended load)
 F. Alluvial roughness equation G. Sediment flux equation between bottom layer and water stream

2.2 Discretization, Solution for Algebraic System and Boundary Condition

The above seven equations for fully coupled non-equilibrium sediment transport model are discretized using the Preissmann scheme of implicit finite difference. In applications of the Preissmann scheme, it is supposed that all the function $f(Z, Q, Z_b, C)$ in the discretized algebraic equations are known at time

level $n\Delta t$ and are differentiable with respect to Z , Z_b , Q and C . Using a Taylor series expansion, the finite difference approximation leads to a system of four algebraic equations for every pair of points $(i, i+1)$. One can obtain the linearized system for a pair of adjacent points $(i, i+1)$. The system of four algebraic equations is solved for all computational points by the double sweep method which is often used to solve the St. Venant equations in fixed bed modeling. The looped network has the points of confluence and divergence of tributaries or canals. Double sweep method is applied for the problem of confluence and divergence because of Cressin reservoir.

2.3 Model Application

The simulated results of mobile bed unsteady flow model are compared with the measurement using the Manning roughness coefficient, n . To estimate n value for mobile bed, the soil conservation service (SCS) method is used as a basic n ($=0.02$) for initial value. After the model calculate n value with van Rijn formula as a basic n and additional n is added to basic n considering channel irregularity. (French, 1986)

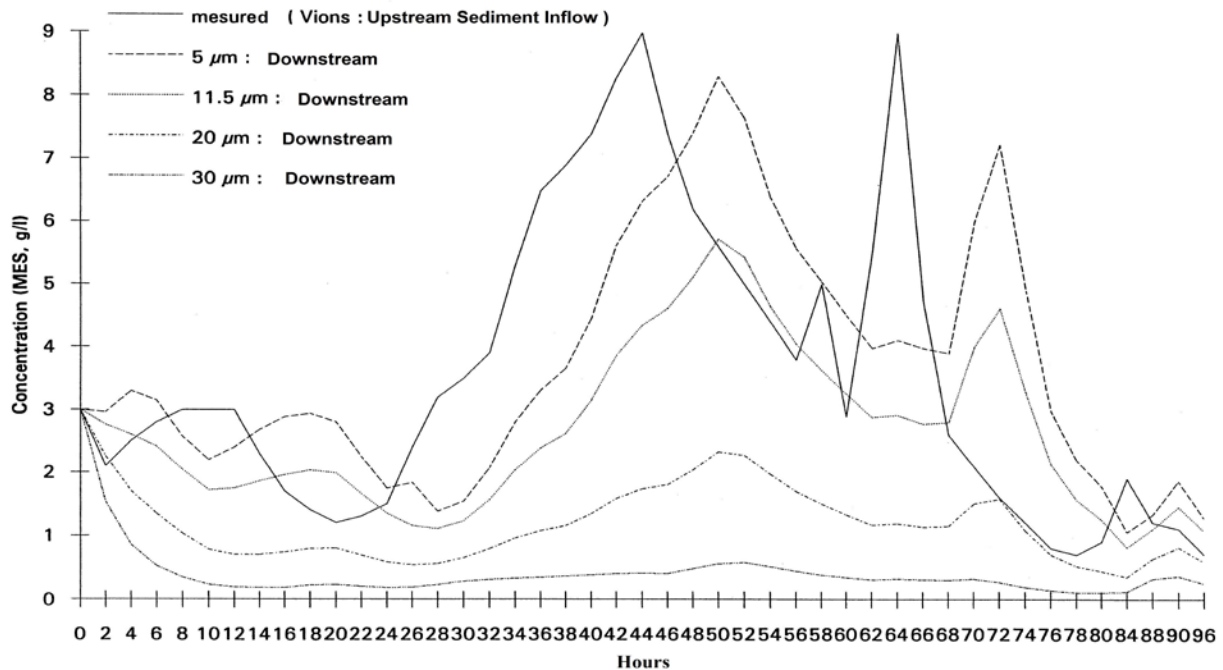
The size distribution for bed material and suspended load are:

Bed material: $D_{16} = 0.034$ mm, $D_{50} = 0.150$ mm, $D_{84} = 0.288$ mm, $D_{90} = 0.375$ mm

Suspended load: $D_{16} = 3.4$ μm , $D_{50} = 11.5$ μm , $D_{84} = 28.0$ μm , $D_{90} = 36.0$ μm

The flushing operation in 1990 is lasted about 4 days. The discharge during 4 days changes with minimum $Q = 512$ m^3/s and maximum $Q = 990$ m^3/s . During flushing the concentration variation is observed with minimum $C = 0.7$ g/l and maximum $C = 9$ g/l . The simulation result of concentration variation for 5 μm , 11.5 μm , 20 μm , and 30 μm are given in the following figure. (Figure 4)

Figure 4. Concentration Variation at Downstream Depending on Sediment Diameter



3. Results and Discussion

The simulation result shows that $D = 5 \mu\text{m}$ is almost transported to downstream, but $D = 30 \mu\text{m}$ is almost deposited in reservoir. Suppose that sediment inflow is $295,000 \text{ m}^3$ and the size distribution is classified four classes such as $D = 5 \mu\text{m}$ (30 %), $D = 11.5 \mu\text{m}$ (30 %), $D = 20 \mu\text{m}$ (20 %) and $D = 30 \mu\text{m}$ (20 %), the total trap efficiency is obtained as follows: (Table 1).

Trap efficiency = deposit/inflow = $119,000 / 295,000 = 40 \% = 0.4$

TABLE 1. Trap Efficiency of Sediment

Diameter(μm)	Inflow(m^3)	Deposit(m^3)	Outflow(m^3)	Trap(%)
5.0	295,000	3,000	292,000	1
11.5	295,000	84,000	211,000	28
20.0	295,000	201,000	94,000	68
30.0	295,000	284,000	31,000	89

4. Conclusions

A fully coupled one-dimensional sediment transport model for unsteady flow and non-equilibrium condition with looped network is created. It is applied to the Belley reservoir of Rhone River in France.

The results of simulation of this model show that $D = 5 \mu\text{m}$ is almost pass through the reservoir and $D = 30 \mu\text{m}$ is deposited about 89 % in the reservoir. The trap efficiency of simulation (=0.4) gives reasonably good result comparing with the measurement (=0.49) in 1990.

This model can be applicable for the non-equilibrium condition such as flushing where D_{50} of bed material is different from D_{50} of inflow sediment.

5. References

- Armanini, A., and Di Silvio, G. (1988). "A One-dimensional model for the transport of a sediment mixture in non-equilibrium condition.", *J. of Hydraulic Research*, Vol. 26, No. 3, pp. 276-286.
- Cunge, J.A., Holly, F.M. Jr, Verwey, A. (1980). *Practical aspects of computational river hydraulics*, Pitman.
- French, R.H. (1986). *Open-channel hydraulics*, McGraw-Hill.
- Holly, F.M. Jr, and Rahuel, J.L. (1990). "New numerical/physical framework for mobile-bed modelling.", *J. of Hydraulic Research*, Vol. 28, No. 4, pp. 404-411.
- Lee, S.H. (1993). *Modelisation numerique du transport solide en ecoulement non-permanent*. Thesis presented to Institut National Polytechnique de Grenoble (INPG) in partial fulfillment of the requirements for the Doctor degree (in French).

Van der Berg, J.A., and van Gelder, A. (1993). "Prediction of suspended bed material transport in flows over silt and very fine sand.", *Water Resources Research*, Vol. 29, No. 5, pp. 1401-1403.

Vanoni, V.A. (1977). *Sedimentation Engineering*, ASCE Task Committee.

Van Rijn, L.C. (1984). "Sediment transport: Part I. Bed load transport." *J. of Hyd. Div.*, ASCE, Vol. 110, No. 10, pp. 1431-1452.

Van Rijn, L.C. (1984). "Sediment Transport: Part II. Suspended load transport." *J. of Hyd. Div.*, ASCE, Vol. 110, No. 11, pp. 1613-1638.

Van Rijn, L.C. (1984). "Sediment transport: Part III. Bed forms and alluvial roughness" *J. of Hyd. Div.*, ASCE, Vol. 110, No. 12, pp. 1749-1754.

Van Rijn, L.C. (1988). "Application of sediment pick-up function." *J. of Hyd. Div.*, ASCE, Vol. 112, No. 9, pp. 1749-1754.

Session 15. Advances in Integrated Modeling

Developing Water Quality Objectives for Diversions to Agriculture from the San Joaquin River using Steady-state (Hoffman) and Transient (CSUID) Models

Nigel W.T. Quinn PhD, P.E.¹, Ayman H. Alzraiee PhD², Charlie Mathiot¹, Karl E. Longley PhD, P.E.²

¹ Berkeley National Laboratory, 1 Cyclotron Rd., MS 64-209, Berkeley, CA 94720, USA. nwquinn@lbl.gov, charlie.mathiot@agroparistech.fr.

² Center for Irrigation Technology, California State University, Fresno, 5730 North Chestnut Street, Fresno, CA 93740. ayman.alzraiee@gmail.com, karll@csufresno.edu.

Abstract

The relationships between agricultural applied water salinity, leaching fraction, and soil salinity are complex. A general understanding is needed to provide decision support to stakeholders and regulators to set realistic salinity objectives for irrigation diversions so that farmers can maintain long-term crop root zone salt balance and protect salt sensitive crops from a decline in yield. The steady-state (Hoffman) salinity spreadsheet model requires a minimum of data inputs and provides easy-to-understand model output based on algorithms developed by the FAO in the 1970's. A new graphical user interface was developed for both the transient Colorado State University Irrigation Drainage model (CSUID) and the Hoffman model to overcome limitations of the steady-state Hoffman model and facilitate inter-comparison of the two models. The user interface facilitates information exchange between the two models and allows the model results to be superimposed. This has allowed stakeholders and regulators a means of transitioning between a simple and more complex model while retaining an overall understanding of the hydrological and salinity dynamics of the Basin. This paper reviews the design and application of the two models and discusses the challenges of simultaneously estimating appropriate leaching fractions for salt sensitive crops grown on salinity-impaired soils on the wide of the San Joaquin Basin, California. The analysis provides suggested salinity criteria for irrigation water supply to afford full protection from potential salinity-induced yield decline. Future use of this decision support system is discussed in the context of drought conditions and salt loading regulation in the San Joaquin Basin.

Keywords

salinity, steady-state model, transient model, crop yield, real-time salinity management

1. Introduction

During the irrigation process and depending on the salt content of the applied water, salts can be both precipitated within the soil or dissolved into the irrigation water as it passes through the soil profile. Salinity, or salt stress, adversely affects a number of high-value salt sensitive crops. When water high in salt content is used to irrigate crops, salinity increases in the crop root zone because the root water uptake concentrates the salt around the roots as pure water is consumed by the plant. Crop growth suppression is more typically related to the total salt concentration than the concentration of a specific ion, although specific ion toxicity effects can occur in certain crops (Hoffman, 2010). Salinity is usually measured as an equivalent electrical conductivity (EC) in units of dS/m, uS/cm or mmhos/cm – being both reproducible and easy to measure in the field. The salt tolerance of crops continually changes over the course of a

season - most crops are very tolerant during germination while the plant lives on seed reserves and becomes sensitive during root emergence. Crops slowly become more tolerant as they progress through the later stages of growth. Salts that contribute to high salinity are water soluble, easily transported by water flux. They can therefore be leached by precipitation or sufficient irrigation water, which moves salts to deeper soil depths past the root zone, when no drainage barriers are present within the salt profile (Hoffman, 2010). In the San Joaquin River Basin (SJR), drainage water returns to the San Joaquin River (SJR) with a higher EC, creating potential conflict between upstream and downstream users and a need for accommodation among agricultural, municipal and wetland stakeholders. The EC of diverted irrigation water supply determines the viability of growing salt sensitive crops grown in the lower SJR and South Delta and the resultant total acreage of these higher value crops. EC objectives were established on the SJR at the downstream Vernalis compliance station by the California State Water Resources Control Board to protect South Delta riparian diverters. Later, in 2004, the Central Valley Regional Water Quality Control Board (CVRWQCB) adopted a water quality control program which called for establishment of upstream salinity objectives to protect downstream riparian diverters. The first phase of the control program established a compliance schedule for achieving River salinity objectives at Vernalis. In the second phase the Basin Water Quality Control Plan will be amended and a program of implementation for salinity management using the upstream salinity compliance objective (CVRWQCB, 2016) initiated.

2. Modeling

Models can help predict the relationships between applied water salinity, leaching fraction, and soil salinity, therefore allowing authorities to set river salinity objectives to help riparian agricultural diverters establish sustainable best management practices that balance water application rates (to leach the salts from the crop root zone) and the salinity of the applied water. Currently used salinity models are either 'steady-state', meaning that they are time-independent and require constants as inputs or 'transient', time dependent and in need of time series inputs. Steady-state models are generally simpler, require less data and are easier to run and calibrate. Transient models are more complex and account for factors such as changes in weather, irrigation and crop selection. Steady-state analyses provide excellent first approximations over long periods of time or in specific conditions like the bottom of the root zone (Hoffman, 2010). Transient models are designed to account for management interventions such switching between crops with different salt tolerances, variable irrigation water salinity, rainfall, multiple years of drought, timing and amount of irrigation, multiple soil layers, crop evapotranspiration (ET). They do not require initial soil salinity to be reset each year.

2.1. Colorado State University Irrigation and Drainage Model (CSUID)

The CSUID model is a three dimensional groundwater flow and salinity model that considers irrigation timing and drainage architecture for individual crop requirements. The model was developed in the late 1980's and used for compare drainage technologies to reduce the concentration of salts in drainage discharge (Alzairee and Garcia, 2013). The model solves the one-dimensional Richards equation and utilizes the advective-dispersive equation for one-dimensional vertical flow and salt transport in the soil profile above the water table. The model is capable of solving the depth-averaged Boussinesq equation and two-dimensional advective-dispersive transport equation for areal flow and transport in the fully saturated zone below the water table – however the simple 1-D model formulation was used in the current application. The model predicts multiple crop stresses such as water deficit, water excess, and salinity while allowing for spatial and temporal variability of three dimensional soil parameters that include hydraulic conductivity, dispersivity, porosity, specific yield and storativity. By tracking the crop root zone over time - CSUID allows assessment of salinity impacts to crop yield at various crop growth stages and during periods of greater salt

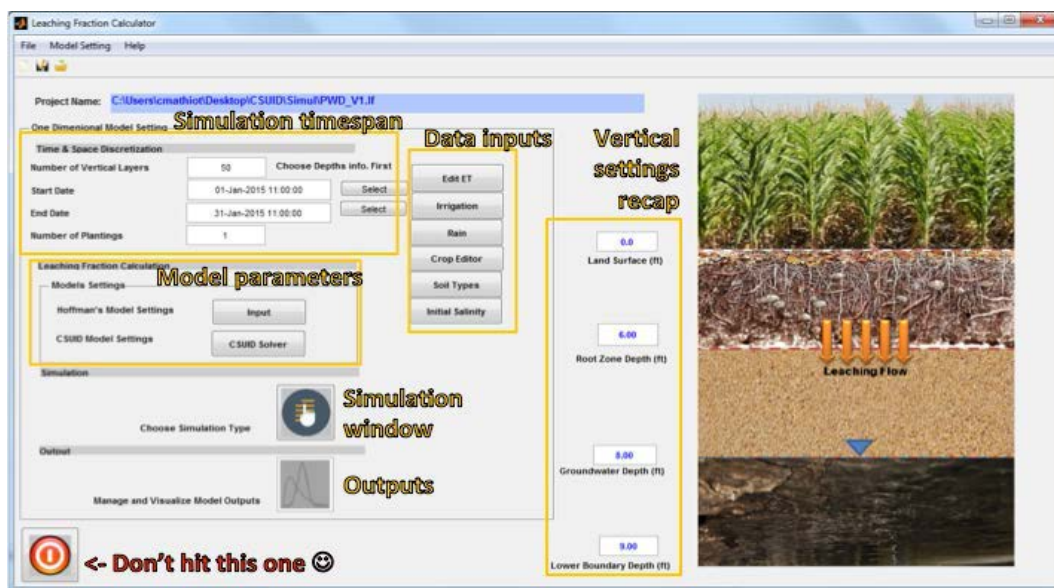
sensitivity. The model has been configured to serve as a decision support tool for developing upstream SJR salinity objectives by determining a limit to irrigation water supply EC that would protect 95% of crops grown in the lower SJRB approximately 95% of the time. The main objective of the project was to develop a robust, user-friendly graphical user interface to CSUID aimed at stakeholder use of the tool for decision making and validation of the recommended EC objective at an upstream compliance monitoring location.

2.2 CSUID/Hoffman Model Graphical User Interface

To be of utility as a decision support tool we required a graphical user interface (GUI) that could be navigated intuitively by stakeholders and where data required to run the model were readily accessed by model users. The topology of the simulation domain appears in Figure 1 and is divided into subject areas for (a) simulation setup, (b) data inputs, (c) soil vertical profile assignment, (d) Hoffman steady-state model parameters, (e) a simulation setup window and (f) output specification. The simulation setup dashboard sets the simulation period by prompting the user to choose start and end dates and the number of crop plantings. CSUID considers crops such as alfalfa that are harvested multiple times during the season as having plantings equivalent to the number of cuttings. For the vertical profile settings only three values are actually needed (land surface is set to 0 ft by default) - elevations for the bottom of the root zone, the average water table depth and the bottom of the soil layer (which is the base of the shallow aquifer or the maximum depth from which tile drains intercept groundwater).

The ‘resolution’ of the simulation can be improved by increasing the number of layers simulated (the higher the number of layers, the higher the precision, but also the longer the computation time). The default value of 50 layers is a good compromise for most vegetable and cereal crops (with a 6m model depth and 50 layers, the width of each layer is approximately 12 cm). Soil infiltration characteristics for each layer are supplied using the “Rosetta soil database” based on soil texture (Alzairee and Garcia, 2013). The parameter values are mean values derived from the literature. Where data are available from field samples – these data can be substituted for the generalized literature values.

Figure 1. User interface for the CSUID 1-D model. Model input templates are accessed directly from this screen view.



The first three buttons of the input dashboard open similar interfaces allowing the user to load weather data. The fourth and fifth buttons are used to set the crop and soil features respectively. The sixth button invokes a dialog box which prompts for details of the initial soil salinity profile. The panel on the left has a spreadsheet format that allows the user to enter and edit data by hand. The number of rows mirrors the simulation interval. The acquired ET data are entered into the second column and are expressed in mm (or inches) /day. English units are used by default in CSUID to make it easier for model users in the USA to understand the data requirements of the model and to reduce the potential for error if the user isn't familiar with metric unit equivalents. For longer simulations, it is much more time-efficient to import the data from an Excel spreadsheet that has been previously formatted. If there is no ready source of evapotranspiration (ET) data (such as proximity to a web-accessible CIMIS station) the model can estimate the ET based on temperature and radiation data previously loaded into the Hoffman model input data interface. Selecting the button on the interface will cause the table to be filled in automatically. In instances where irrigation schedules are not readily available, an estimated irrigation schedule can be developed based on the ET, rain and crop data, previously loaded. The interface allows the user to enter all the data related to the crop that is being grown using the model simulation. The Hoffman steady-state model parameters are supplied to the model from the dashboard labelled "Model Parameters". The spreadsheet form of the Hoffman model is typically a trial-and-error solution whereby the leaching rate is defined and the analyst manipulates the allowable soil salinity through annual applied water salinity, given inputs of annual precipitation while keeping yield response above a minimum acceptable level. The CSUID model provides two options for output comparison with the Hoffman model— one that uses the actual leaching rates provided by the analyst and a second that uses daily leaching rates calculated by the CSUID model. Analysis and comparison of these model outputs will allow an eventual transition from the generalized and somewhat conservative steady-state Hoffman modeling approach to the more realistic transient modeling approach provided by CSUID.

3. Results

3.1 Hoffman Model Results

Hoffman model data was gleaned from irrigation consultants operating in water districts that divert water from the SJR. Hoffman model output from these data show that at leaching fractions of 0.20 and 0.25, average soil water salinity does not exceed the tomato salt threshold of 5.0 deciSiemens when applied irrigation salinity is between 0.0 and 2.5 deciSiemens per meter; as a result relative crop yield will not fall below 95%. However at a leaching fraction of 0.15, average soil water salinity exceeds the tomato crop threshold of 5.0 deciSiemens per meter when applied irrigation salinity exceeds 2.1 deciSiemens per meter when annual precipitation is taken into account and 2.0 deciSiemens per meter when annual precipitation is not taken into account. However at a leaching fraction of 0.15, relative yield decreases below 95% when annual rainfall is below four inches. Hoffman model simulations show that at leaching fractions of 0.20 and 0.25 irrigation water salinity of 2.5 deciSiemens per meter would protect at least 95% of tomato crops. Similarly at a leaching fraction of 0.15 and irrigation water salinity of 2.0 deciSiemens per meter - 95% of tomato crops would be protected.

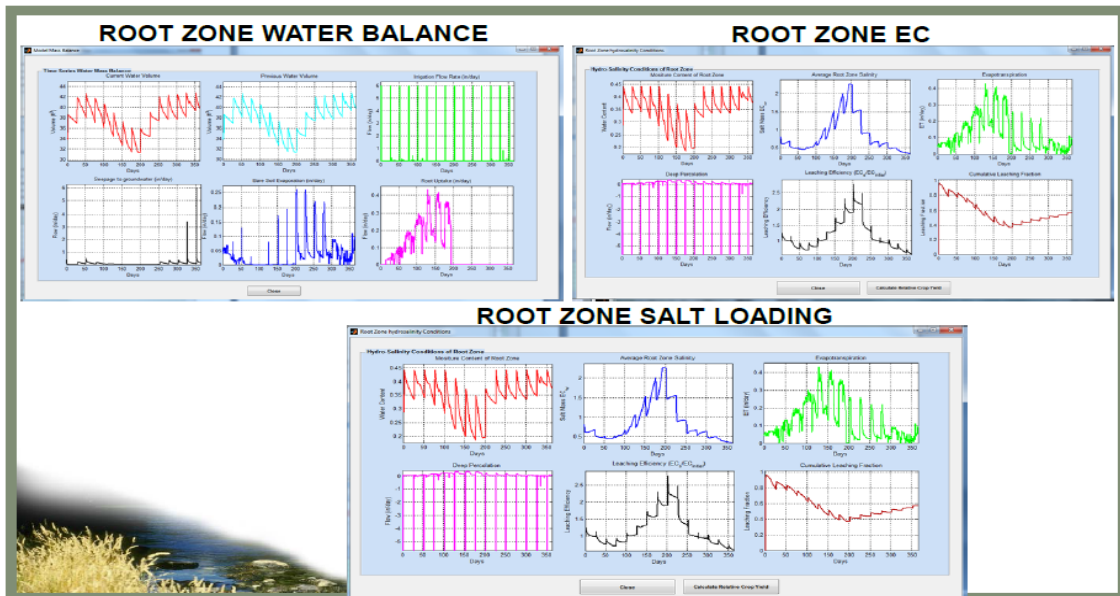
Soil properties such as soil salinity continually change with the application of irrigation water and effective precipitation can be significantly influenced by the timing of precipitation events. These time dependent factors can affect crop yield. A factor that the Hoffman model does not adequately consider is the initial salinity profile of the area of interest – the spreadsheet model assumes that the soil profile returns to an initial state at the end of the irrigation season. High soil content or the presence of residual soluble salts in the soil profile can cause a loss in crop yield regardless of the applied irrigation salinity. The Hoffman model

also fails to account for saline soil conditions at different depths, which may increase average root zone soil water salinity depending on the site-specific properties, such as the upward movement of shallow groundwater. However, the Hoffman model uses data inputs that are easily located, adequately measured, and can be applied to regional areas. Accordingly, the Hoffman model is able to estimate the necessary irrigation water salinity to protect crop yields for large areas of interest with a high degree of reliability despite its limitation as a decision support tool.

3.2 CSUID Model Results

Average root zone salinity was the easiest model output that could be directly compared for the CSUID and Hoffman models. Average root salinity surpassed the tomato salt threshold at two periods during the CSUID simulation. The average root zone salinity over the entire simulation was 2.4 dS/m. The first period, March 1st to March 22nd, was most likely due to the dissolution of salinity in the soil root zone before adequate leaching could occur. The second period, from July 12th to August 2nd, could be attributed to an increase in evapotranspiration leading to an increased concentration of salt within the crop root zone. The increases in salinity above tomato threshold concentration would not occur in soils where the existing salt content of the root zone was much lower. It is possible that the study site had unusually saline soil given that the farmers were attempting to optimize production on land that had a history of salinity problems. It could be argued that the study site soils were not sufficiently reclaimed. The CSUID model salinity output suggests potential yield impacts based on the limited irrigation application and EC data available that are not evident in the Hoffman steady-state model output. Figure 2 shows the graphical output for root zone salinity balance, root zone salinity and root zone salt loading for the same scenario analyzed with the Hoffman steady-state model.

Figure 2. CSUID output showing root zone water balance, EC and salt load for tomato crop.



4. Conclusions

The steady-state Hoffman spreadsheet model embedded in the user interface was used to engage stakeholders and develop an upstream SJR salinity objective that would be protective of 95% of crops grown in the Basin approximately 95% of the time. The CSUID transient salinity model and graphical user interface provide decision support for stakeholders to manage root zone salinity dynamically. The new user interface facilitates information exchange between the two models and allows the model results to be compared directly within a common analytical framework. More importantly from a modeling perspective - it allows stakeholders and regulators a mechanism for transitioning between simple and more complex models while retaining an overall understanding of the hydrological and salinity dynamics of the Basin. The CSUID model also helps define the continuous input data required to run and calibrate the model – many of these data such as real-time irrigation water delivery data and the EC associated with these deliveries – are not commonly collected by water districts. It is our belief that this level of salinity management, guided by the transient CSUID model, will be needed for sustainable irrigation with saline water supply and recycled drainage – especially as soil salinity approaches the salt tolerance of agricultural crops grown in the Basin.

5. References

- Alzraiee, A H., Gates, T. K., & Garcia, L. A. (2013). Modeling Subsurface Heterogeneity of Irrigated and Drained Fields. II: Multivariate Stochastic Analysis of Root-Zone Hydrosalinity and Crop Yield. *Journal of Irrigation and Drainage Engineering*, 139(10), 809–820. [http://doi.org/Doi 10.1061/\(ASCE\) Ir.1943-4774.0](http://doi.org/Doi 10.1061/(ASCE) Ir.1943-4774.0)
- Central Valley Regional Water Quality Control Board. 2016. Revisions to the 2010 salt tolerance of crops in the Lower San Joaquin River (Merced to Stanislaus River Reaches) and 2016 Addendum, Final Report. April, 2016.
- Hoffman, G. J. 2010. Salt Tolerance of Crops in the Southern Sacramento-San Joaquin Delta. Final Report to Central Valley Regional Water Quality Control Board.

Session 16. Environmental Flows Modeling Under Climate Extremes

Using Machine Learning to Statistically Model Natural Flow: The Sacramento Watershed under Dry Conditions

Bonnie R. Magnuson-Skeels¹, Jay R. Lund¹, Robert J. Hijmans¹, Theodore E. Grantham²

¹ University of California Davis, One Shields Avenue, Davis, CA, USA. For correspondence, contact brmagnuson@ucdavis.edu.

² University of California Berkeley, 35 Mulford Hall, Berkeley, CA USA.

Abstract

Machine-learning techniques were applied to climatic, geologic, and geographic data to statistically model natural flow in dry years, and preliminary results are presented. The dry-year natural flow model builds on a general-purpose statistical natural flow model developed by the US Geological Survey designed to be able to predict natural flows at the national and regional scale. Such models can be used when building a traditional mechanistic natural flow model is too expensive or time-consuming. Applying multiple machine-learning algorithms, using different techniques to select features and reduce dimensionality, and restricting training data to drier years resulted in models that, when used to predict known dry water year flows and evaluated on multiple test metrics, generally tested as better than or equivalent to the corresponding general-purpose models. In certain cases, they performed far better. This represents an improvement in predicting natural flows for dry years.

Keywords

Natural flow, machine learning, statistical learning, Sacramento River

1. Introduction

Calculating a river's natural or unimpaired flow is a difficult problem (Arthington *et al.*, 2006), but it is often useful to have an estimate of a river's natural or unimpaired flow. It can be done in several mechanistic or statistical ways. Mechanistic models include building a detailed watershed model based on physical hydrologic principles and historic, "pre-disturbance" records of flow as well as using observed streamflow from current gage measurements and "unimpaired" them by adding known diversions back in. Statistical models start with known data about the variable of interest (in this case, flow rate) and other variables thought to be relevant. They then apply statistical principles to tease out a relationship to predict the "expected" value for the variable of interest. Statistical models can be simpler and faster to put together than mechanistic models, particularly if predictor variables (such as elevation or rainfall) are readily available (Eng *et al.*, 2012).

Statistical modeling, also known as machine learning, has often been used to predict observed hydrology, but its application to prediction of expected natural flows is more recent. Researchers at the US Geological Survey (USGS) have effectively used random forests to predict natural flow at ungaged locations based on available geospatial data (Carlisle *et al.*, 2010). A version of this model has been used as input to the Drought Water Rights Allocation Model (DWRAT), a water rights curtailment model developed at the University of California, Davis as a research project for the California State Water

Resources Control Board (Grantham, 2014). DWRAT takes estimates of full natural flow for various points throughout a watershed and, given data on local water rights, uses formal optimization methods to suggest ideal curtailments if available water is insufficient (Lord, 2015; Lund *et al.*, 2014).

DWRAT’s curtailment decisions can only be as good as the natural flow model that supports them. Past work has made the natural flow model more accurate, but it is worthwhile to evaluate and to improve its accuracy for estimating dry-year flows. This research made use of additional machine learning algorithms, additional methods to select features (x-variables) and reduce their dimensionality, and training the model on more applicable datasets (a dataset of only dry-year flows and a dataset of only flows from the Sacramento Basin) to try to improve the natural flow model’s predictions for dry-year flows in the Sacramento watershed. The Sacramento watershed was focused on because a Sacramento River version of DWRAT is currently in development. The results showed that stacking machine learning models on top of each other tended to improve predictive accuracy, as did using a dry-year dataset for certain areas of the Sacramento watershed.

2. Methods

The original USGS flow model uses random forests to predict average flow rate in cubic feet per second (cfs) based on publicly available geospatial data. The y-variable (also known as the label, response variable, or dependent variable) is flow as recorded by reference gages in the GAGES II database (Carlisle *et al.*, 2010). The x-variables (also known as features, predictor variables, or independent variables) are climatic, geologic, and geographic data such as precipitation, temperature, elevation, and soil characteristics calculated for the location of each reference gage for 1950-2011. These are used to train a set of 36 monthly regional models—12 monthly models for each of California’s 3 aggregated ecoregions (Coastal, Intermountain, and Xeric)—and can then be used to predict for any location in California (Grantham, 2014).

This research started from the same data, although it only used data from the Intermountain and Xeric aggregated ecoregions because of the focus on the Sacramento watershed. Two main scenarios were examined: using the monthly-regional approach of the USGS model but restricting each training set to dry years, and creating a single model based on all data available for locations in the Sacramento basin. Five-fold cross-validation was used to evaluate model performance on unseen test data. For the Sacramento basin scenario, traditional five-fold cross-validation was sufficient. However, ensuring model comparability to test if a dry-year dataset resulted in a more accurate model than an all-year dataset was more complicated. To evaluate the dry-year dataset approach, data from drier years was randomly shuffled and split into 5 different 80%/20% train/test sets. For a given fold, anything in the full dataset not in the dry-year test set was then treated as the all-year training set. The dry-year test sets were used as a “universal test set” that the dry-year and all-year training sets could be evaluated against to see if the dry-year restriction improved predictive accuracy. See Figure 1.

Each dataset was sent through a standardized sequence to try out combinations of models and versions of that dataset. Datasets were scaled from 0 to 1, an approach that can be helpful for some machine learning models. The set of predictor

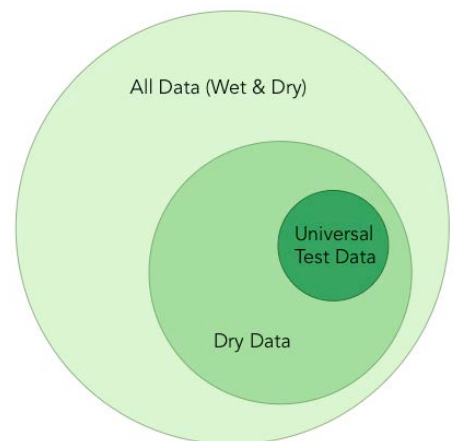


Figure 1. Venn Diagram of Dry-Year/All-Year Dataset Partitioning

variables in each version of the dataset (unscaled and scaled) was then reduced using four approaches: two sizes of Principal Components Analysis to reduce their dimensions yet keep their information, a variance threshold technique that only retained x-variables that varied sufficiently relative to each other, and retaining a list of specific x-variables chosen based on their definitions as being most likely to impact natural flow. For the dry-year scenario, this resulted in 20 different versions of the dataset. For the Sacramento basin scenario, since it did not start with two versions of the same dataset, it resulted in 10 different versions of the dataset.

A set of nine different machine learning algorithms were then tuned for each dataset, meaning their parameters were calibrated to optimal values based on the results of a grid search across the chosen parameter space using five-fold cross-validation of the training set to estimate performance. The machine learning models chosen were ridge regression, random forests, k-nearest neighbors, support vector machine, decision tree, AdaBoost, and three second-level ensemble models: averaging the predictions of these six, stacking their predictions and feeding them in as x-variables to a second-level predictor (referred as a “stacking ensemble”), and using the stacking ensemble approach but also including the original x-variables as input to the second-level model. For a given month in a given region in the dry-year scenario, these 9 algorithms combined with the 20 datasets meant there were 180 algorithm-dataset combinations whose performance could be compared against each other. Each trained algorithm was then applied to its matching testing dataset to find the best approach for predicting natural flow and evaluated on 5 different performance metrics: R-squared, mean and standard deviation of the observed/expected ratio, mean squared error, and root mean squared error. Averaging these results across the 5 folds gave a cross-validated estimate of how a model would perform on an unseen dataset.

3. Results

To evaluate the dry-year approach, the sequence was run for every month for both the Intermountain and Xeric ecoregions. This resulted in 24 best models (chosen by highest cross-validated R-squared value). Stacking models were most often chosen as the best algorithm, although random forests and k-nearest neighbors also performed well. These new best models generally showed improvement in the performance metrics relative to the original USGS model when it was run through the exact same cross-validation process. See Figure 2 for the improvement in Intermountain ecoregion performance results in R-squared and mean observed/expected ratio.

The new monthly Intermountain models had an R-squared value closer to 1 than the USGS model for each month, and their mean O/E value was closer to 1 in most months. This demonstrates the increased accuracy of the new best models. Reducing the training data to dry years often improved performance in the Intermountain ecoregion, contributing to the increase in R-squared values in Figure 2. However, a reduced, dry-year dataset was rarely part of the best dataset-algorithm combination in the Xeric ecoregion. As shown in Figure 3, the Xeric region’s best models did not show as dramatic an improvement in R-squared, although it was higher for most months. Results for the new models’ mean observed/expected ratio were mixed, improving for half of the months but worsening for the other half.

Figure 2. Intermountain Region: Comparison to USGS Models Dry-Year Performance

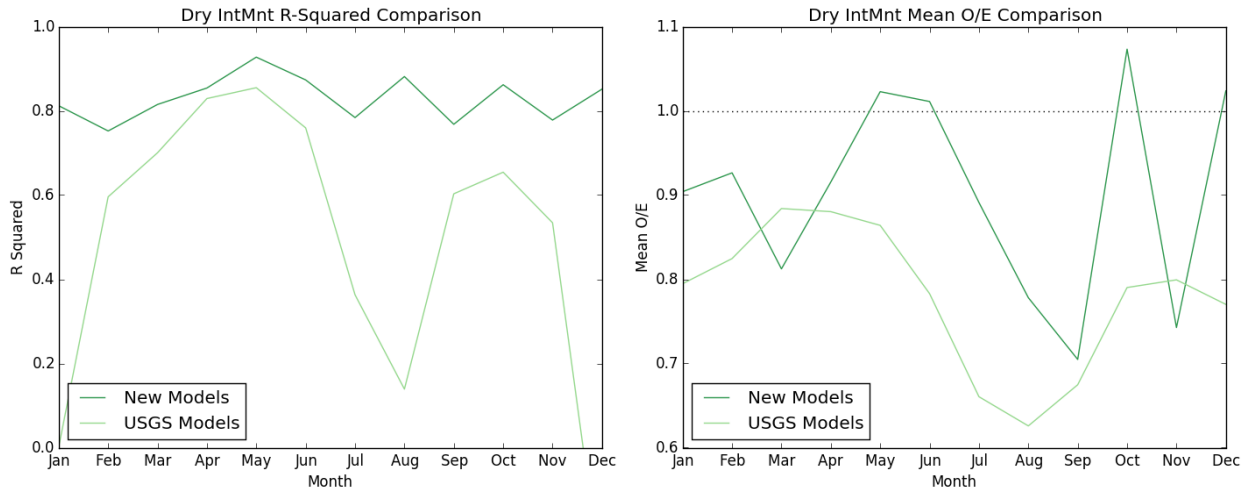
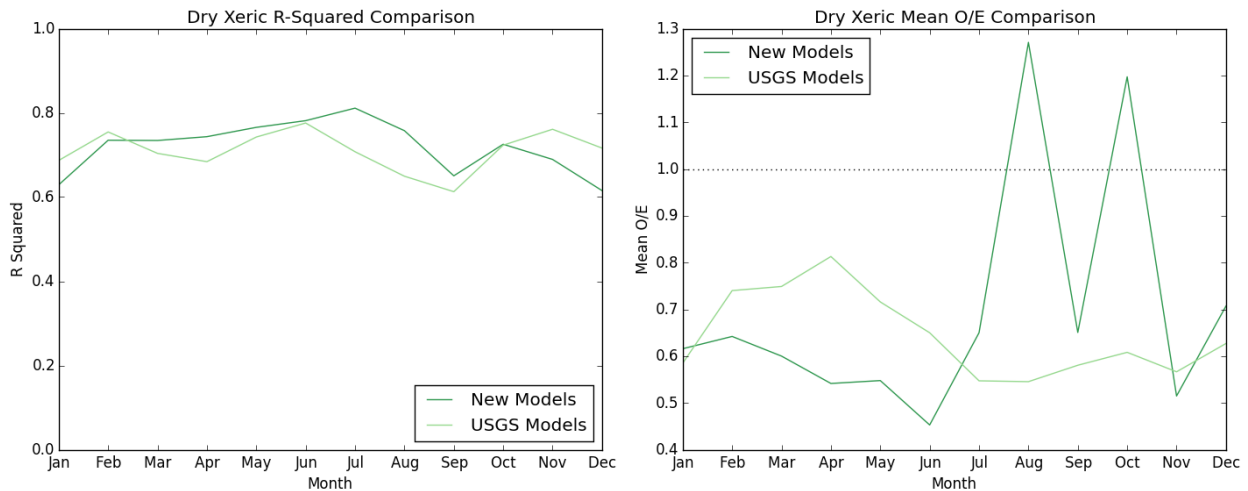


Figure 3. Xeric Region: Comparison to USGS Models Dry-Year Performance



The difference between regions in whether or not restricting the data to dry years was helpful is interesting. The monthly Intermountain scenarios often benefitted from training on a dry-year dataset, demonstrating that using a more targeted dataset to train the model can be helpful. The main exceptions were the high-runoff spring months, which likely see more variable flows. Perhaps this is because training the model on the complete dataset gave the model more variable examples from which to learn. In contrast, the dry-year monthly Xeric scenarios did not benefit from using a more curated dataset in most months. The wet-year/dry-year disparity in the Intermountain region is probably much greater than in the Xeric region. Given this, including wet years in the dataset when training a model to predict for dry years in the Xeric region probably does not bias model predictions as strongly toward wet years as it seems to in the Intermountain region.

Restricting the training data geographically to only reference gages within the Sacramento basin resulted in a model that scored well on test data. However, it tended to predict unrealistically low flows,

probably because the training dataset was made up of only 11 gages, most of which are located above the rim of the Sacramento basin.

4. Conclusions and Future Research

The original USGS random forest models seem to perform relatively well for dry year natural flow prediction, but they can be improved. The approach of creating a set of monthly regional models performed best. Training the Intermountain models on a dry-year dataset—a improvement first suggested by Carlisle *et al.* (2010) in the original presentation of the USGS model—improved performance, although it was not helpful in the Xeric ecoregion. The use of stacking ensemble modeling also provides a useful boost in predictive accuracy. These improvements suggest that using the new models would possibly improve the ideal curtailments suggested by the Sacramento River DWRAT.

The new natural flow models perform well on the test data, but they should also be assessed on their performance for the main stem of the Sacramento River. Both the new models and the original USGS models share the limitation of being trained on data from a particular type of location. Training the model to predict for those locations does not mean it will predict well for all locations, as Carlisle *et al.* (2010) also indicated. Evaluating how well the model expands from being able to predict for smaller streams and upper reaches of large rivers to being used to predict for the main stem of a large river is the next step in the ongoing work for this research.

5. References

- Arthington, A. H., Bunn, S. E., Poff, N. L., & Naiman, R. J. (2006). The Challenge of Providing Environmental Flow Rules to Sustain River Ecosystems. *Ecological Applications*, 16(4), 1311-1318.
- Carlisle, D. M., Falcone, J., Wolock, D. M., Meador, M. R., & Norris, R. H. (2010). Predicting the Natural Flow Regime: Models for Assessing Hydrological Alternation in Streams. *River Research and Applications*, 26(2), 118-136.
- Eng, K., Carlisle, D. M., Wolock, D. M., & Falcone, J. A. (2012). Predicting the Likelihood of Altered Streamflows at Ungauged Rivers across the Conterminous United States. *River Research and Applications*, 29(6), 781-791.
- Grantham, T. E. (2014). *Appendix B Section 2 (Drought Water Rights Allocation Tool Supply Estimation) of Drought Curtailment of Water Rights: Problems and Technical Solutions* (pp. 6). Center for Watershed Sciences: University of California, Davis.
- Lord, B. (2015). Water rights curtailments for drought in California: Method and Eel River Application. (Master of Science Thesis), University of California, Davis.
- Lund, J., Lord, B., Fleenor, W., & Willis, A. (2014). *Drought Curtailment of Water Rights: Problems and Technical Solutions* (pp. 23). Center for Watershed Sciences: University of California, Davis.

Session 18. San Joaquin River Restoration Program 2D Hydraulic Modeling Applications

Two-dimensional Water Temperature Modeling of In-channel and Hydraulically Connected Off-channel Zones in Reach 1A of the San Joaquin River

Daniel E. Dombroski¹, Blair Greimann², Yong Lai³

¹ Bureau of Reclamation, Technical Service Center, Denver, CO, USA, ddombroski@usbr.gov

² Bureau of Reclamation, Technical Service Center, Denver, CO, USA, bgreimann@usbr.gov

³ Bureau of Reclamation, Technical Service Center, Denver, CO, USA, ylai@usbr.gov

Abstract

The San Joaquin River Restoration Project (SJRRP) Office of Reclamation has requested the Technical Service Center (TSC) analyze water temperature dynamics in Reach 1A of the San Joaquin River. A desired outcome of the SJRRP is to restore and maintain fish populations in “good condition” in the mainstem San Joaquin River below Friant Dam to the confluence of the Merced River, including naturally reproducing and self-sustaining populations of salmon and other fish. Water temperature is affected by input flow conditions and local meteorology; the presence of large hydraulically connected off-channel pools in Reach 1A potentially complicates the local thermal dynamics, impedes fish passage, and provides refuge for predatory species. A module in development at the TSC for computing two-dimensional water temperature dynamics was adapted for application to Reach 1A of the San Joaquin River. The water temperature module is coupled to the SRH-2D computational software package, which contains a two-dimensional flow and mobile bed sediment transport solver. The two-dimensional temperature model of Reach 1A of the San Joaquin River was generally successful in predicting spatial and temporal thermal dynamics within the system and may be useful in predicting habitat suitability, predation potential, and ultimately for informing management decisions.

Keywords

hydraulic, temperature, modeling, thermal, dynamics, habitat, salmonid, restoration, off-channel

1. Introduction

A primary objective of the San Joaquin River Restoration Project is to restore and maintain fish populations in “good condition” in the mainstem San Joaquin River below Friant Dam to the confluence of the Merced River, including naturally reproducing and self-sustaining populations of salmon and other fish. The survival of young salmonids is highly dependent on appropriate water temperature during the period they occupy the river system. Water temperature is affected by input flow conditions and local meteorology. Historically, the San Joaquin River harbored the southernmost runs of Pacific coast salmon. The warm climate of the San Joaquin Valley combined with management practices along the riparian corridor challenge efforts to maintain adequate water temperatures in the warm months of the year.

The San Joaquin River Restoration Project (SJRRP) Office of Reclamation has requested the Technical Service Center (TSC) analyze water temperature dynamics in Reach 1A of the San Joaquin River. Reach 1A just downstream of Friant Dam has been identified for potential spawning habitat. The presence of large hydraulically connected off-channel pools in Reach 1A potentially complicates the local thermal dynamics, impedes fish passage, and provides refuge for predatory species. A module in development at the TSC for computing two-dimensional water temperature dynamics was adapted for application to Reach 1A of the San Joaquin River. The water temperature module is coupled to the SRH-2D computational software package, which contains a two-dimensional flow and mobile bed sediment transport solver. An existing hydraulic model for the reach was used as a basis for the coupled hydraulic and water temperature model.

Based upon comparisons with data from temperature monitoring sites located within the channel and off-channel zones in Reach 1A, the two-dimensional temperature model was generally successful in predicting spatial and temporal thermal dynamics. The model will likely be useful in predicting habitat suitability and predation potential within the system, and ultimately for informing management decisions and guiding restoration design.

2. Methods and Case Study

The temperature solver (Lai & Mooney, 2009) is coupled to the existing SRH-2D flow and sediment transport model (Lai Y. G., 2010). Hydraulic variables are computed by solving the depth-averaged dynamic wave equations using a finite volume numerical method. With appropriate boundary conditions, constant or varying discharge flows may be simulated. The temperature module solves, at the same time interval as the hydraulic solver, an additional two-dimensional depth-averaged conservation equation,

$$\frac{\partial hT}{\partial t} + \frac{\partial hUT}{\partial x} + \frac{\partial hVT}{\partial y} = \frac{\partial}{\partial x} \left[\frac{hv_t}{\sigma_t} \frac{\partial T}{\partial x} \right] + \frac{\partial}{\partial y} \left[\frac{hv_t}{\sigma_t} \frac{\partial T}{\partial y} \right] + \frac{\Phi_{net}}{c_w \rho_w}, \quad 1$$

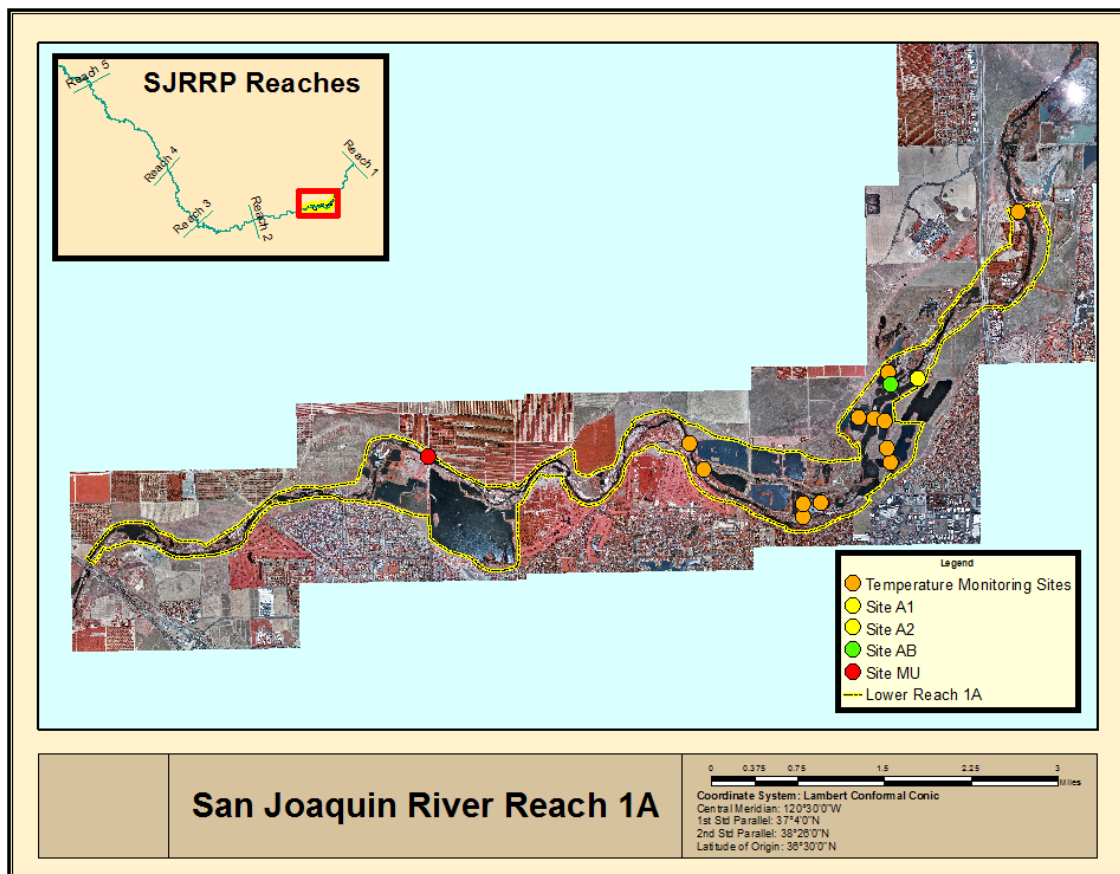
where T is depth-averaged water temperature, x and y are horizontal Cartesian coordinates, t is time, h is water depth, U and V are depth-averaged velocity components in x and y directions, respectively, v_t is the turbulent viscosity, σ_t is the turbulent Prandtl number, ρ_w is the water density, c_w is the specific heat of water, and Φ_{net} is the net heat exchange into the water column. The net heat exchange,

$$\Phi_{net} = \Phi_{ns} + \Phi_{na} + \Phi_{bed} - \Phi_{br} - \Phi_e - \Phi_c, \quad 2$$

is a function of solar radiation entering the water surface, Φ_{ns} ; atmospheric radiation entering the water surface, Φ_{na} ; heat loss by back radiation from the stream, Φ_{br} ; evaporative heat loss at the water surface, Φ_e ; conductive heat loss at the water surface, Φ_c ; and heat flux into the stream at the channel bed, Φ_{bed} . Theoretical details of how to evaluate contributions to the net heat exchange (Equation 2) are given in Lai & Mooney (2009) and Dombroski et al. (2016).

The Reach 1A project section of the San Joaquin River below Friant Dam from approximately the Highway 41 bridge (SJRRP mile post 255) to the Highway 99 bridge (SJRRP mile post 243) features a particularly large number (relative to other SJRRP reaches) of abandoned off-channel gravel pits which are hydraulically connected to the main stem river at low to moderate flow rates (Figure 1). The hydraulic and temperature effects of the connected pools on habitat characteristics are of particular interest to the SJRRP.

Figure 1. San Joaquin River Reach 1A study site showing delineated boundaries of temperature model (yellow), extending from SJRRP Mile Post 255 (Highway 41 Bridge) to SJRRP Mile Post 243 (Highway 99 Bridge). Also shown are the location of temperature monitoring points (colored circles). The reach contains numerous off-channel hydraulically-connected pools due to historic gravel mining operations; the presence of the pools is expected to complicate restoration actions within the reach due to hydraulic and water quality effects on potential habitat.



The temperature modeling described herein is based upon prior two-dimensional hydraulic modeling of Reach 1A; computational mesh development and calibration and validation of the hydraulic model are described elsewhere (Gordon & Greimann, 2014).

Temperature in the river has been continuously monitored by statically-located data loggers; some are positioned in the off-channel pools and some are positioned in-channel. Figure 1 shows the location of temperature monitoring probes within the modeled river section. Data from monitoring points was used for calibration and validation of the temperature model.

The heating source terms (Equation 2) in the temperature solver are driven by temporal records of measured or predicted meteorological data. For initial calibration and validation simulations, measured meteorological and solar data was derived from a combination of CIMIS station data at Fresno State University and California ASOS Network METAR data at Fresno Air Terminal. For subsequent model

testing of water-year type hydrographs, the meteorological data was derived from National Climatic Data Center (NCDC) hourly normals and solar data was derived from the National Solar Radiation Database (NSRD).

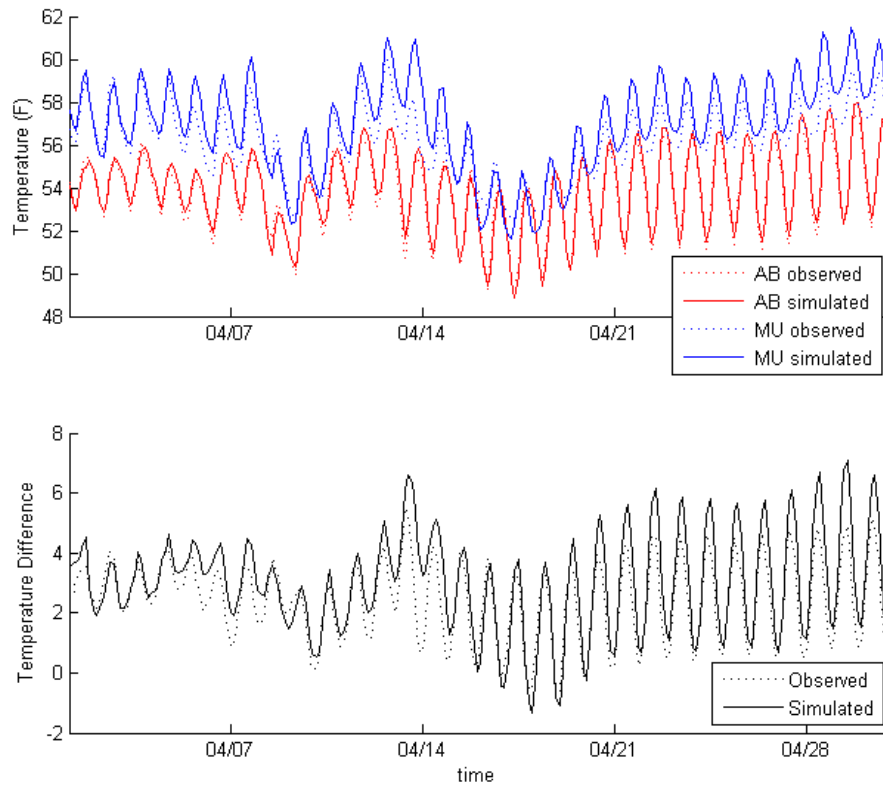
For time-dependent (unsteady) simulations, a hydrograph and water temperature record specify the inlet boundary conditions to the model. The temperature record is based on the measured temperature at the nearest upstream monitoring point (Figure 1) during the period of simulation. The initial temperature and hydraulic distributions within the system were setup by calibrating the model for a one month (simulation time) duration prior to the validation simulations. This initial “break-in” period of simulation is necessary in order to inundate all the hydraulically connected regions within the mesh and to setup a physically realistic temperature distribution that reflects a natural hydrograph with seasonal and diurnal weather fluctuations. The model was then run for a one month (simulation time) validation period under four different six-week-long hypothetical hydrographs. The hydrographs are specified in the stipulation of settlement (NRDC vs. Rodgers: Stipulation of Settlement, 2006) for varying water-year types (wet, normal, dry, and critical). Further details on model setup, calibration, and validation are given in Dombroski et al. (2016).

3. Results and Discussion

The sensitivity of the simulated water temperature to variation in meteorology and input parameters (Equation 2) was tested by comparing temporal records of predicted temperature at points within the channel and off-channel pools. Based on the temperature differential between trials, simulated water temperature in the off-channel hydraulically-connected zones is more sensitive than the in-channel flow to variation in meteorology and empirical parameters that drive the heating terms (Equation 2). The sensitivity is a function of the much longer residence time of off-channel flow compared to in-channel flow. The in-channel flow temperatures are driven primarily by the convective transport of heat from the upstream water (Friant Dam tailwater), whereas the off-channel pool temperatures are determined in part by a historical integration of local meteorology. For this reason, water temperature (both observed and simulated) in the off-channel zones is significantly warmer than the in-channel flows, which are fed by the relatively cold bottom release from Friant Dam. The sensitivity tests also showed that the simulated water temperature is more sensitive to variation in meteorological conditions than to variation in the parameterization of the heat source terms, an encouraging result because it indicates robust ability of the model to simulate physical processes. Presented in Figure 2 **Error! Reference source not found.** and Figure 3 are results of validation tests of simulated water temperature records compared to observed conditions for points at in-channel and off-channel zones, respectively.

The temperature trends within the channel measurement locations (Figure 2) represent an observation at one point within the water column. It is assumed that turbulent mixing in the channel is sufficient that the water column is well-mixed in the vertical dimension. In the well-mixed case, the point observation in the water column converges to depth-averaged water temperature, allowing for physically meaningful comparison between observed and simulated temperature. The observed temperature trends within the off-channel pools (Figure 3) indicate the presence of vertical temperature gradients, due to commonly observed physical processes in lakes and reservoirs. The lower monitoring point observes colder, slowly varying temperature, while the upper monitoring point observes warmer, rapidly varying temperature. A more thorough set of observations in the vertical dimension at the measurement locations would be required in order to calculate and directly compare a depth-averaged observed temperature to the simulated water temperature.

Figure 2. Simulated water temperature compared to observed water temperature at in-channel points AB and MU located near the upstream and downstream extents, respectively, of the modeled reach. The upper plot shows water temperature (observed vs. simulated) at the points AB and MU. The lower plot shows the temperature difference (MU-AB), indicative of the warming that occurs through the reach.



In order to predict the effect of proposed conditions on water temperature, an additional simulation was performed for water-year type hydrographs stipulated in the restoration settlement (NRDC vs. Rodgers: Stipulation of Settlement, 2006). Figure 4 and Figure 5 present simulated water temperature records for each of the water-year type hydrographs at an in-channel location and an off-channel pool, respectively. The response at the in-channel location demonstrates that the water-year type hydrograph may be responsible for large variation in water temperature within the channel. Water temperature in off-channel hydraulically-connected zones are affected in a much smaller way by variation in water-year type. An exception to this generalization is demonstrated by large inundation events which increase the connectivity of the off-channel zone with the flows in the channel. This is evident in the wet water-year type scenario (Figure 5) when the hydrograph discharge increases to almost 4000 cfs, producing a larger flow through the off-channel pool area and a dramatic reduction in water temperature.

Figure 3. Simulated water temperature (red) compared to observed water temperature (black) at point A located in an off-channel pool adjacent to the channel point data presented in Figure 2. Observed water temperature is given at two vertical locations in the water column.

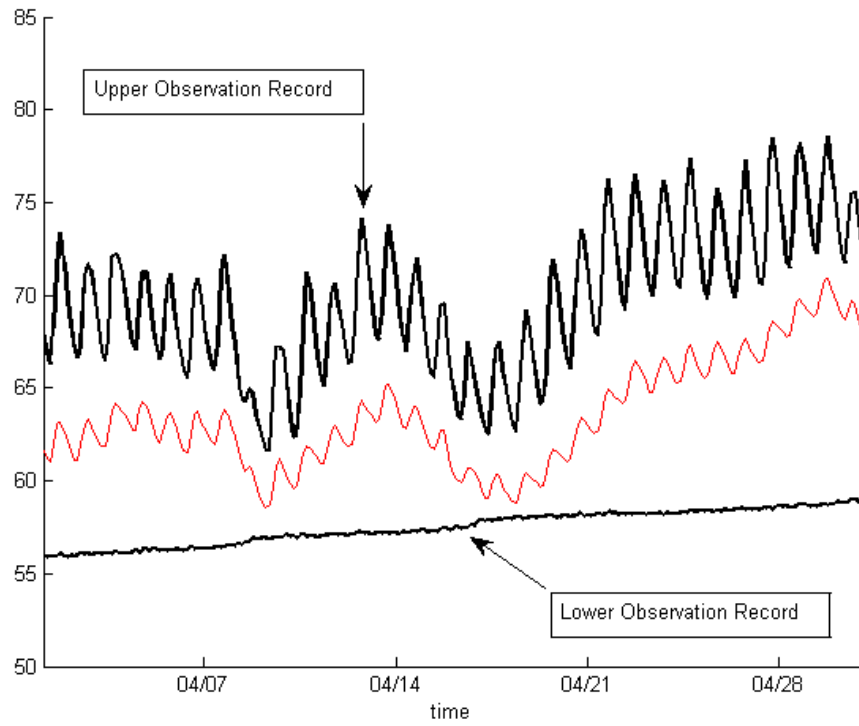


Figure 4. Comparison of simulated water temperature at an in-channel point (AB) for variation in water-year type hydrographs as stipulated in the restoration settlement (NRDC vs. Rodgers: Stipulation of Settlement, 2006).

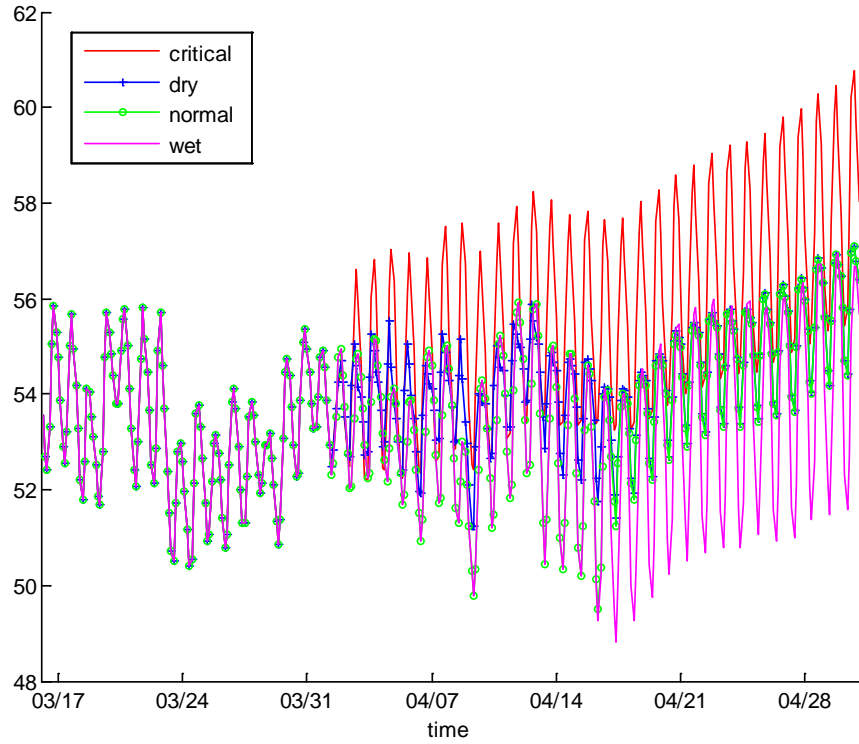
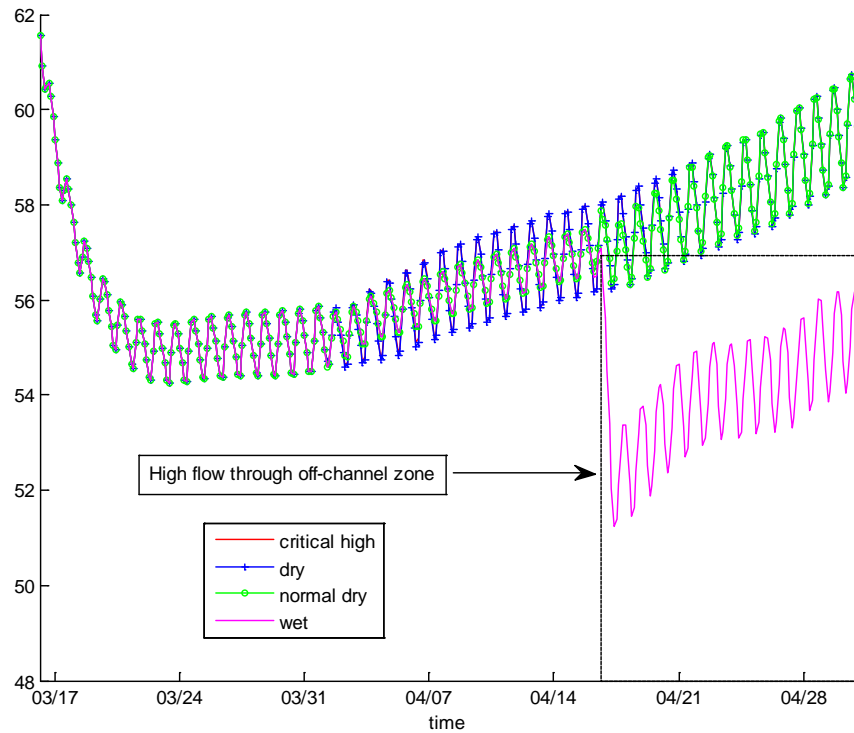


Figure 5. Comparison of simulated water temperature at a point (A1) in an off-channel pool for variation in water-year type hydrographs as stipulated in the restoration settlement (NRDC vs. Rodgers: Stipulation of Settlement, 2006)



4. Conclusions

A model in development at the TSC for computing two-dimensional water temperature dynamics was adapted for application to Reach 1A of the San Joaquin River. Water temperature is affected by input flow conditions and local meteorology; the presence of large hydraulically-connected off-channel pools in Reach 1A potentially complicates the local thermal dynamics, impedes fish passage, and provides refuge for predatory species. Simulation results indicate that the water temperature dynamics in off-channel hydraulically-connected pools may be very different than temperature dynamics in the channel. Water temperature in off-channel pools is highly dependent on meteorological conditions, whereas in-channel temperature is driven primarily by the flows entering at the upstream end. Based upon comparisons with data from temperature monitoring sites located within the channel and off-channel zones, the two-dimensional temperature model was generally successful in predicting spatial and temporal thermal dynamics. The model will likely be useful in predicting habitat suitability and predation potential within the system, and ultimately for informing management decisions and guiding restoration design. Monitoring data indicate the presence of vertical temperature gradients in the off-channel pools which limits the applicability of a depth-averaged model to reproduce the physical processes involved. Additional monitoring and analysis would be required to quantitatively resolve the temperature gradients and provide a relation to the simulated depth-averaged temperature.

5. References

- Dombroski, D. E., Greimann, B., & Lai, Y. (2016). *Two-dimensional water temperature modeling of in-channel and hydraulically connected off-channel zones in Reach 1A of the San Joaquin River*. Denver: Bureau of Reclamation.
- Gordon, E., & Greimann, B. (2014). *Two-Dimensional Modeling of Reach 1A of the San Joaquin River between Friant Dam and Highway 99*. Denver: Bureau of Reclamation, Technical Service Center.
- Lai, Y. G. (2010). Two-Dimensional Depth-Averaged Flow Modeling with an Unstructured Hybrid Mesh. *Journal of Hydraulic Engineering*, 136(1), 12-23.
- Lai, Y., & Mooney, D. (2009). On a Two-Dimensional Temperature Model: Development and Verification. *World Environmental and Water Resources Congress 2009*, (pp. 1-14). Kansas City, Missouri.
- NRDC vs. Rodgers: Stipulation of Settlement, CIV S-88-1658 LKK/GGH (United States District Court September 13, 2006).

Session 20 Poster Session

The Need for a Physically Based and Simple Estimation of MODFLOW's River Conductance Parameter (CRIV)

Hubert Morel-Seytoux¹, Cinzia Miracapillo², Steffen Mehl³ and Calvin Miller⁴

¹ Hydroprose Int. Consult, 328 Beech Avenue, Santa Rosa, USA, hydroprose@sonic.net

² Fachhochschule Nordwestschweiz, Switzerland, politec1@yahoo.com

³ Chico State University, Chico, California, USA, smehl@csuchico.edu

⁴ Miller Groundwater, Fort Collins, Colorado, USA, calvin@millergroundwater.com

Abstract

Flow exchange between streams and ground water is of great importance, be it for beneficial allocation and use of the water resources or for the proper exercise of water rights. In large-scale regional studies many numerical models treat the water table aquifer as a single calculation layer, which makes it difficult to provide a rigorous depiction of the phenomenon. In particular a somewhat arbitrary conductance coefficient in a third type boundary condition is used to calculate the seepage discharge as a function of the difference of head in the river and in the aquifer, whose value is often found by calibration. Recently a different approach was developed to estimate that coefficient analytically. Here the emphasis is to show how that conductance can be estimated when an anisotropic condition holds in the aquifer. Costly numerical calculations are avoided and yet accuracy is attained.

Keywords

Stream-Aquifer Interaction; Flow Exchange; River Coefficient; River Penetration; Anisotropy; Clogging Layer.

1. Introduction

An unresolved problem is how to estimate simply yet accurately the coefficient in a third type boundary condition needed to calculate the seepage discharge from a river when the water table aquifer is treated numerically as a single calculation layer. The goal of this presentation is to alert the reader to better options to estimate CRIV, both those already available and those still in development.

2. Motivation for the Research

For example, in a study for the Santa Rosa Plain Watershed Groundwater Management Plan, the horizontal square grid size is 660 feet and the area under investigation is 262 square miles. None of the rivers in the area have widths that exceed 100 feet. *Thus all river reaches are included in cells that have dimensions far in excess of the river widths.* The water table aquifer, which always exceeds 90 feet of thickness is treated as a single calculation layer in the vertical direction, while the river depths are often no more than a few feet.

In such context the *boundary condition* to determine the seepage discharge, Q , is chosen to be of the *third type*. The discharge is calculated as being proportional to the difference between the head in the river, h_S , and the head in the aquifer, h_a , at the center of the vertical thickness of the cell that contains the river (the river cell). The proportionality coefficient depends upon (1) the length of the river reach, L , within the river cell, (2) the wetted perimeter of the cross-section of the river, W_p , (3) an undefined but usually low hydraulic conductivity in the aquifer near the river bottom, K , and (4) an undefined thickness, e , akin to that of a clogging layer. Symbolically the relation is:

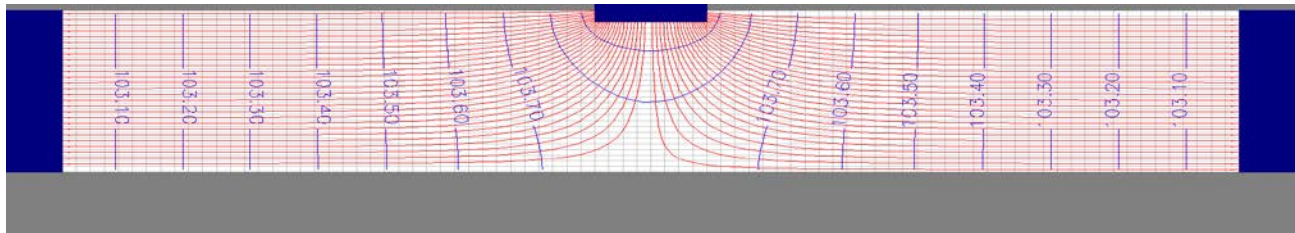
$$Q = \left(\frac{K}{e}\right) (LW_p)(h_S - h_a) = C_{riv}(h_S - h_a) \quad (1)$$

The coefficient $\frac{K}{e}$ is an empirical correction factor (K having dimension of velocity and e that of a length) needed to match observed data. In most groundwater models used commercially, the determination of the coefficient C_{riv} (dimension of transmissivity) is left to the user and most often $\frac{K}{e}$ is estimated by calibration when sufficient historical data are available. There is a need for a more physically based approach.

3. Case of Isotropy in the Aquifer. Methods and Case Studies

The approach has been a combination of analytical derivations and numerical verifications using readily available codes based on the finite-difference or finite-element approximations. Details of these techniques can be found in the cited references. We now simply define the problem, discuss the difficulty to solve it and summarize some results. Note a major difference from the usual approach in typical groundwater models. The head in the aquifer is not evaluated at the center of the river cell but in the case of isotropy at a distance away from the river bank which is *twice* the aquifer thickness. Under isotropic conditions this is, conservatively, the distance required for the flow, which naturally is very much vertical at the river bottom, to become essentially horizontal. See Figure 1 for a visualization of this fact. In other words by that distance the Dupuit-Forchheimer assumption holds. That distance is referred as to as the “(conservative) standard far distance”, normalized l_f divided by the aquifer thickness.

Figure 1. Flow path. Slightly penetrating river. Figure not to scale.



Under isotropic conditions the one-sided discharge, i.e. the discharge from the left or right bank of the river cross-section, is given as:

$$Q_{iso} = \Gamma K_H L (h_S - h_{far}) \quad (2)$$

Q : one-sided (right or left) seepage discharge (volume per time)

Q_{iso} : one-sided (right or left) seepage discharge (volume per time) in case of isotropy

Γ : one-sided SAFE (Stream Aquifer Flow Exchange) dimensionless conductance for the case of isotropy, no clogging layer and the *standard* far distance.

K_H : aquifer horizontal hydraulic conductivity, which in this case equals the vertical one, K_V .

L : length of river reach; h_s : head in the river; h_{far} : head at the far (“enough”) distance, the (*conservative*) *standard* far distance in the horizontal direction.

The value of Γ was obtained analytically and verified numerically (Morel-Seytoux, 2009; Morel-Seytoux et al., 2013; Miracapillo and Morel-Seytoux, 2014).

4. Case of Anisotropy in the Aquifer. Methods and Case Studies

It was postulated that the discharge in the case of anisotropy could be deduced from the value it would have under the case of isotropy. The relation between the two is:

$$Q_{anis} = R_f(\xi)Q_{iso} \quad (3) \quad \text{or equivalently:} \quad \Gamma_{anis} = R_f(\xi)\Gamma_{iso} \quad (4)$$

$R_f(\xi)$ is the reduction factor as a result of the anisotropy in the water table aquifer.

$$\xi = (1 - DOP)(1 - \sqrt{RANIS}); \quad RANIS = \frac{K_V}{K_H}; \quad (5)$$

DOP = Mean depth of river penetration/aquifer thickness, D .

The approach was verified both analytically and numerically. The computer models used for the numerical verification were MODFLOW, IWFEM and a code well used in Switzerland, ASMWIN (Miracapillo and Morel-Seytoux, 2014). Reduction factors were derived analytically for an elliptical cross-section. They are compared to those obtained numerically for rectangular cross-sections. With these preliminary runs the results seem to confirm that as long as the normalized wetted perimeter ($W_p^N =$ wetted perimeter / aquifer thickness) and the degree of river penetration ($dp =$ average river depth in the cross-section/aquifer thickness) are the same, then for practical purposes the shape of the cross-section does not affect much the reduction factor. Comparison between five sets is shown in Figure 2. This is still a preliminary result to be confirmed with additional runs for more extreme situations. In addition there is an important caveat for use of that figure. It assumes that the conservative *standard* far distance in the case of anisotropy is the same as in the case of isotropy. Figure 3 shows that it is not the case. For the case of anisotropy a larger far distance is required before the Dupuit-Forchheimer assumption is met.

Figure 2. Reduction factor as derived by different analytical and numerical approaches

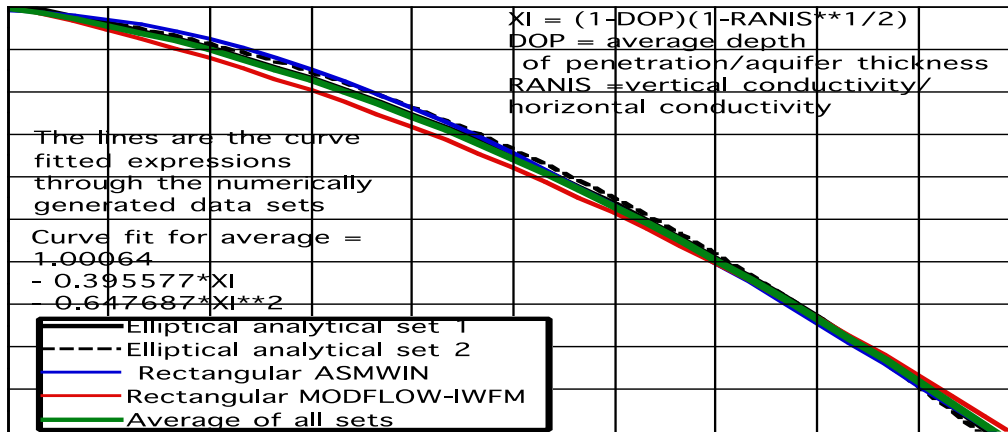


Figure 3. Slightly penetrating river in an aquifer of high degree of anisotropy, $RANIS = 0.01$. The “natural” standard far distance depends upon the degree of penetration and the anisotropy ratio. It increases as the anisotropy ratio decreases. It decreases as the degree of penetration increases. This is shown by comparison of Figure 3 with Figure 4 where the degree of penetration is high and the degree of anisotropy is relatively low. Clearly in that case the flow becomes horizontal quite naturally as it moves away from the river bank.

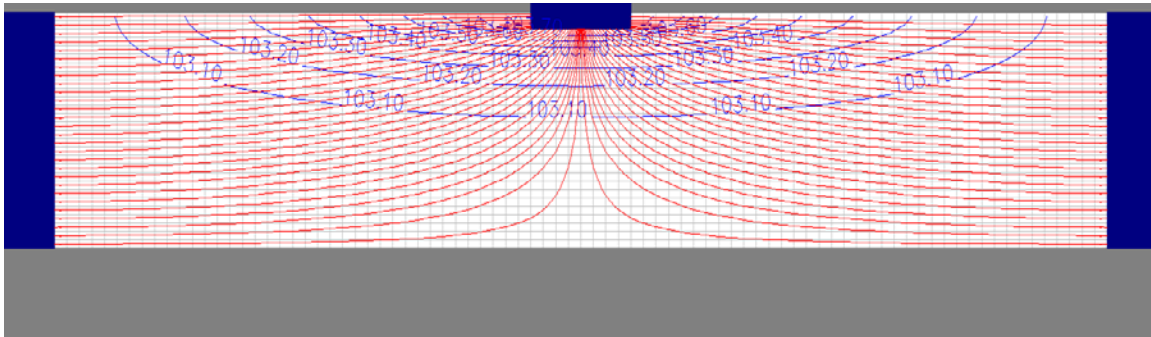


Figure 4. Highly penetrating river in an aquifer of relatively low degree of anisotropy, $RANIS = 0.1$.

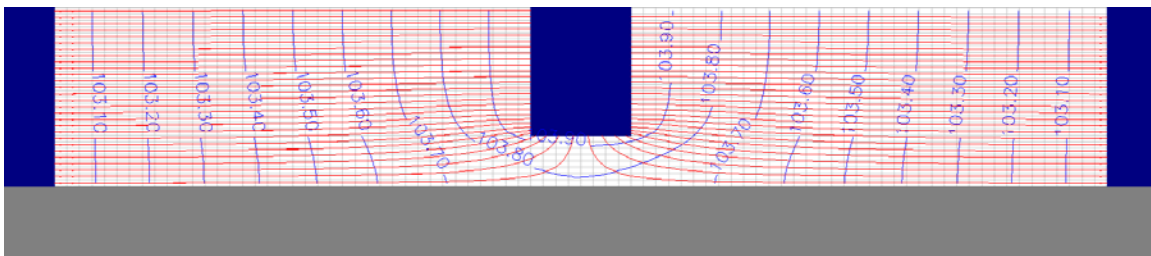
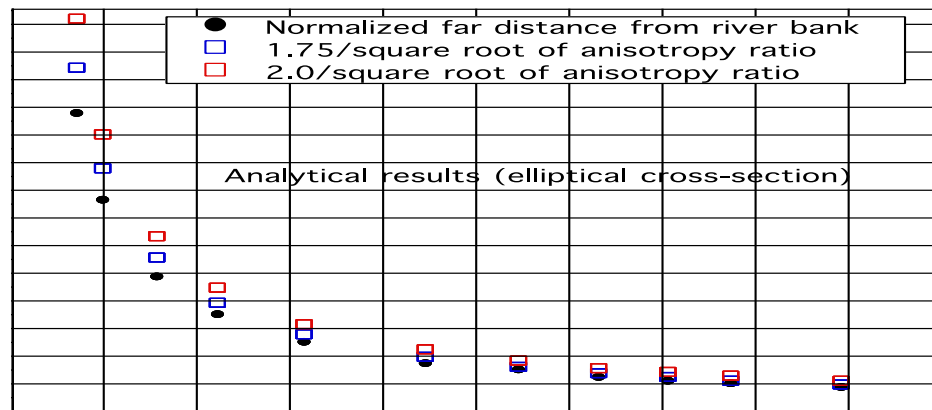


Figure 5 shows how the standard far distance varies with the anisotropy ratio in the case of a more or less “elliptically shaped” cross-section (Morel-Seytoux, 2009). $\rho = \sqrt{\frac{K_V}{K_H}}$. The far distance away from the river bank varies inversely with the square root of the anisotropy ratio, ρ , as theory would suggest (e.g. Muskat, 1937; Carslaw and Jaeger, 1959; Harr, 1962). The black dots in the figure correspond to the analytically calculated values of the normalized far distance from river bank. The result is not standard because for an anisotropy ratio of 1 (isotropic case) and for this particular cross-section it has a value of 1.75 not 2, the latter which is somewhat arbitrary but commonly invoked and more conservative (Morel-Seytoux, 2009). The blue squares display the function $\frac{1.75}{\rho}$. They do not match perfectly the black dots because for an elliptical cross-section it is not possible to have zero degree of penetration as it is for a rectangular cross-section. Thus the black dots were obtained for cross-sections that had degrees of penetration varying between 0.0077 and 0.0153, small but not exactly zero.

Figure 5. Normalized standard far distance as a function of anisotropy



5. Extension for an Arbitrary Far Distance G (in excess of the standard far distance) and a Real Clogging Layer

For practical reasons one is likely to want a far distance (say where the head is calculated in the computation matrix of the numerical code) different than the standard far distance, the difference being denoted Δ . Similarly there might be a real clogging layer with a much lower conductivity than in the aquifer. Corrections are thus necessary (Morel-Seytoux, 2009) leading to a value with the symbol

$$\Gamma_{anis-\Delta-rcl}$$

6. Discussion

The coefficient $C_{riv-SAFE} = \Gamma_{anis-\Delta-rcl} K_H G$ (6) is not identical to the classical C_{riv} say in MODFLOW. A relation has to be deduced between them based on the structure of the finite difference equations used in MODFLOW. The derived relation is simple and algebraic (Morel-Seytoux et al., 2016):

$$C_{riv} = 2GK_H \left\{ \frac{\Gamma_{anis-\Delta-rcl}}{1 - \left(\frac{G}{D}\right)\Gamma_{anis-\Delta-rcl}} \right\} \quad (7)$$

where G is the grid size i.e. the side length of the horizontal square cell and

$$\Delta = G - x \text{ far-anis-standard} \quad (8)$$

The coefficient C_{riv} is definitely a function of the grid size, directly through G but also through $\Gamma_{anis-\Delta-rcl}$ which depends on Δ , which in turn depends on G .

7. Conclusions

The river coefficient (CRIV) is often obtained by calibration in numerical models which have a certain grid size. Yet it is often desirable to use a different grid for later management studies. However the original calibrated river coefficient is no longer valid at that different grid size. Also, in some cases the coefficient must be estimated without the benefit of calibration. The approach presented here allows for better estimation of the coefficient, including the re-estimation of the calibrated river coefficient as the grid size changes.

8. References

- Carlsaw, H. and J. Jaeger, 1959. *Conduction of heat in solids*. Oxford University Press, 510 pages.
- Harr, M.E.(1962). *Groundwater and seepage*. McGraw-Hill book company. New York, 315 pages.
- Morel-Seytoux, H.J. (2009), The turning factor in the estimation of stream-aquifer seepage, *Ground Water*, 47, 205-212, doi: 10.1111/j.1745-6584.2008.00512.x.
- Miracapillo, C., and H. J. Morel-Seytoux. (2014), Analytical solutions for stream-aquifer flow exchange under varying head asymmetry and river penetration: Comparison to numerical solutions and use in regional groundwater models, *Water Resour. Res.*, 50, doi:10.1002/2014WR015456.
- Morel-Seytoux, H.J., Steffen Mehl and Kyle Morgado. (2013), Factors influencing the stream-aquifer flow exchange coefficient, *Ground Water*, 49(5): 775-781. doi: 10.1111/gwat.12112, 7 pages.
- Morel-Seytoux, H.J., Calvin Miller, Steffen Mehl and Cinzia Miracapillo, (March 2016). River seepage conductance in large-scale regional studies. Draft in final stage of preparation.
- Muskat, M. (1937). *The flow of homogeneous fluids through porous media*. McGraw-Hill book company. New York, 763 pages.

Session 25. Dealing with Drought: Data, Modeling, and Strategies

Hydrology of the Recent California Drought and Comparison with Past Droughts

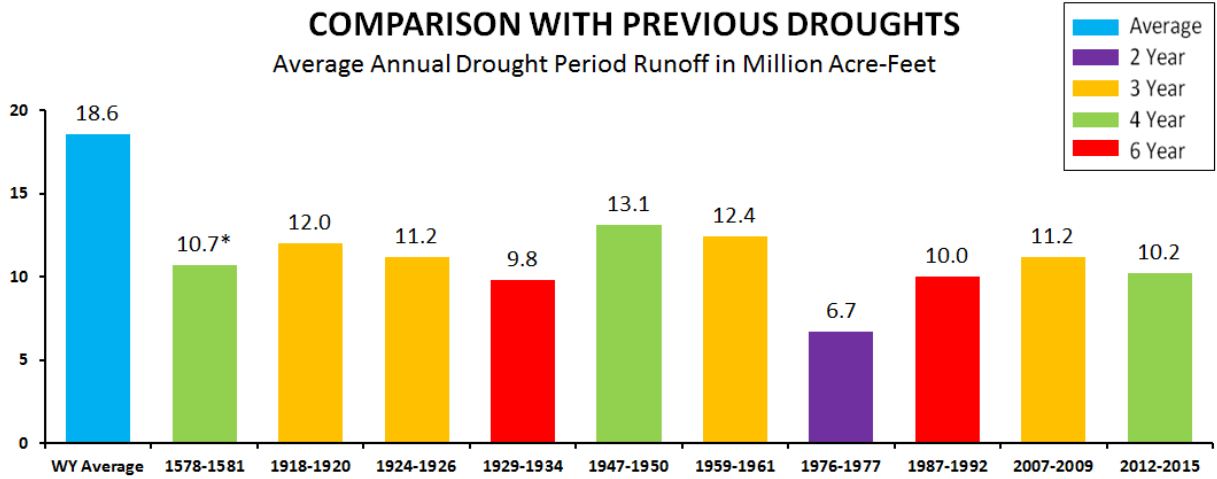
Maurice Roos¹

¹Chief Hydrologist (part time), California Dept. of Water Resources, 3310 El Camino Ave, Room 200, Sacramento, CA 95821, mroos@water.ca.gov

1. Introduction

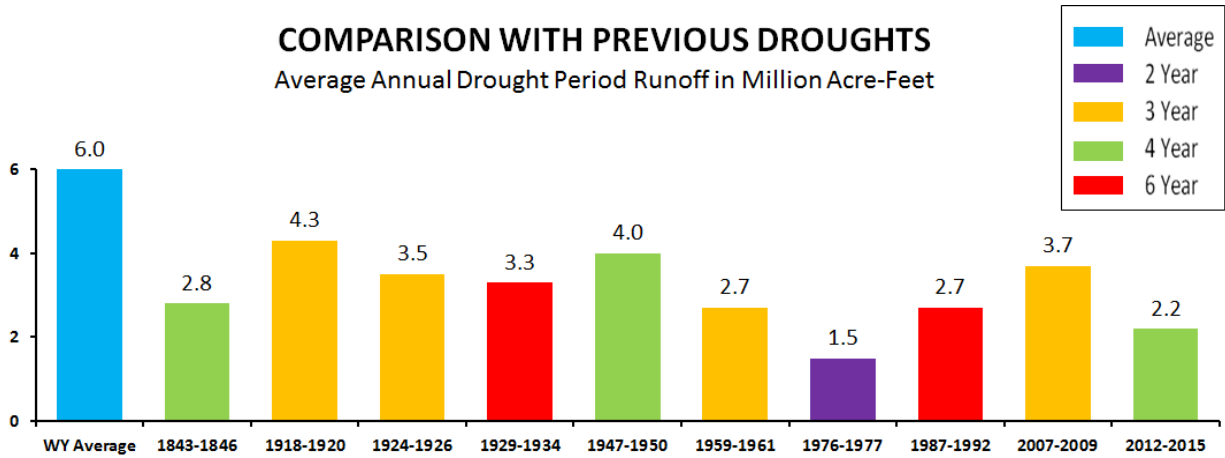
Water years 2012-15 turned out to be a severe 4 year drought in California (and may not be over yet). Other notable droughts of the past 100 years included 1918-1920, 1924-1926, 1929-1934, 1976-1977, 1987-1992, and 2007-2009. Using the Sacramento and San Joaquin River system 8 river runoff as a base, the past year, water year 2014 (WY 2014, October 2013-September 2014), was the 4th driest of the historical record. WY 2015 runoff was about 20 percent more than 2014 on the Sacramento, but worse on the San Joaquin River system where WY 2015 was second driest exceeded only by the severe 1977 year. For the combined 8 rivers, the current water year, October 2014 through September 2015, will probably be the 6th driest in a record of 110 years. The 4 year runoff, WY 2012-15, for the 8 river system will be the driest 4 year set of record, exceeding slightly the previous record of 1931-34. However, on the southern group, the San Joaquin River system, the past 4 years were by far the worst 4 year period in a 114 year record, and about 20 percent drier than any 4 years in a reconstructed record of over 1000 years estimated from tree rings. This drought was most severe across central California, including the Central Coast, San Joaquin Valley, and southern Sierra regions. Figure 1 compares multi-year droughts of the Sacramento and San Joaquin River basins. Figure 2 shows the hydrologic regions of California and the percentages of normal precipitation for the rainy season during the past water year 2014-15, the 4th year of the drought.

Figure 1. Multiyear droughts of the Sacramento and San Joaquin River Basins



SACRAMENTO FOUR RIVER RUNOFF

* from tree rings

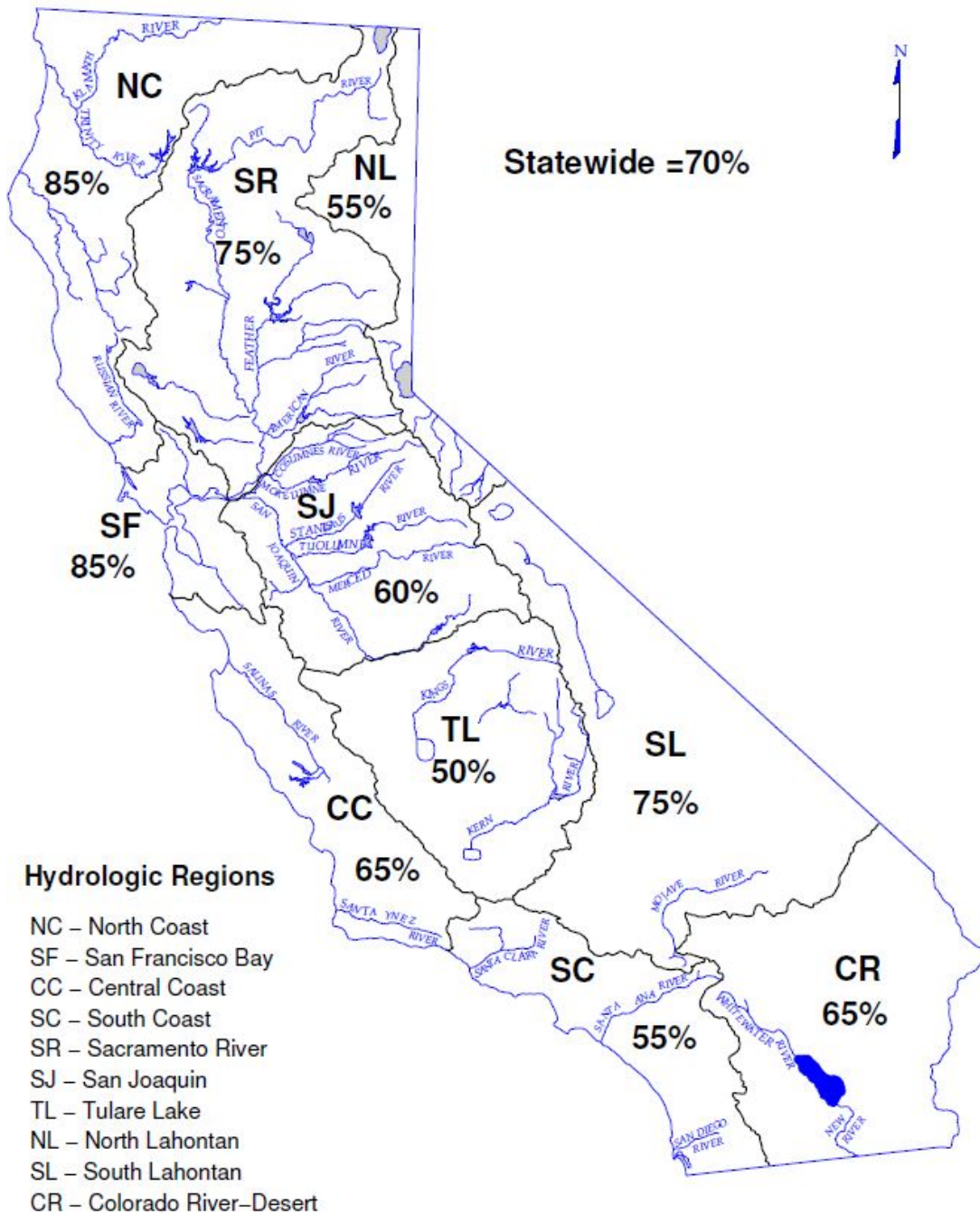


SAN JOAQUIN FOUR RIVER RUNOFF

* from tree rings

Figure 2. California Precipitation for the 2014-15 Rainy Season.

DEPARTMENT OF WATER RESOURCES
CALIFORNIA COOPERATIVE SNOW SURVEYS
SEASONAL PRECIPITATION
 IN PERCENT OF AVERAGE TO DATE
 October 1, 2014 through April 30, 2015



2. Precipitation Deficits

The underlying cause of drought is lack of precipitation. Most of Northern California rainfall occurs during the 5 winter months from November through March. On average about $\frac{3}{4}$ of the yearly precipitation comes then. The third figure, a northern Sierra precipitation bar chart, shows by month what happened during the last 4 water years in the northern Sierra Nevada, our primary water supply region. The horizontal bar gives the monthly average for the 4 recent years in the bar portion of the chart. The first water year, 2011-12 started out poorly, with almost no rain during December, near normal January, and again dry in February with seasonal deficit of about 50 percent at that point and a 30 percent of average snowpack. But March precipitation was triple average with an April 1 snowpack of 50 percent alleviating major concern that year since carryover storage was good coming out of the wet 2011. Water year 2012-13 started well with November and December about twice normal, and led to concerns about floods later in the season. Then the water shut off, with no significant rain or snow for the rest of the year except for one moderate storm in March. That led to the driest calendar year of record during 2013 (See Figure 4 for the 2 year monthly precipitation record). Carryover storage from 2012 was about average and remained near average into early 2013, but would not rise much in spring because of a low 40 percent snowmelt.

Figure 3. Northern Sierra 8 Station Monthly Precipitation

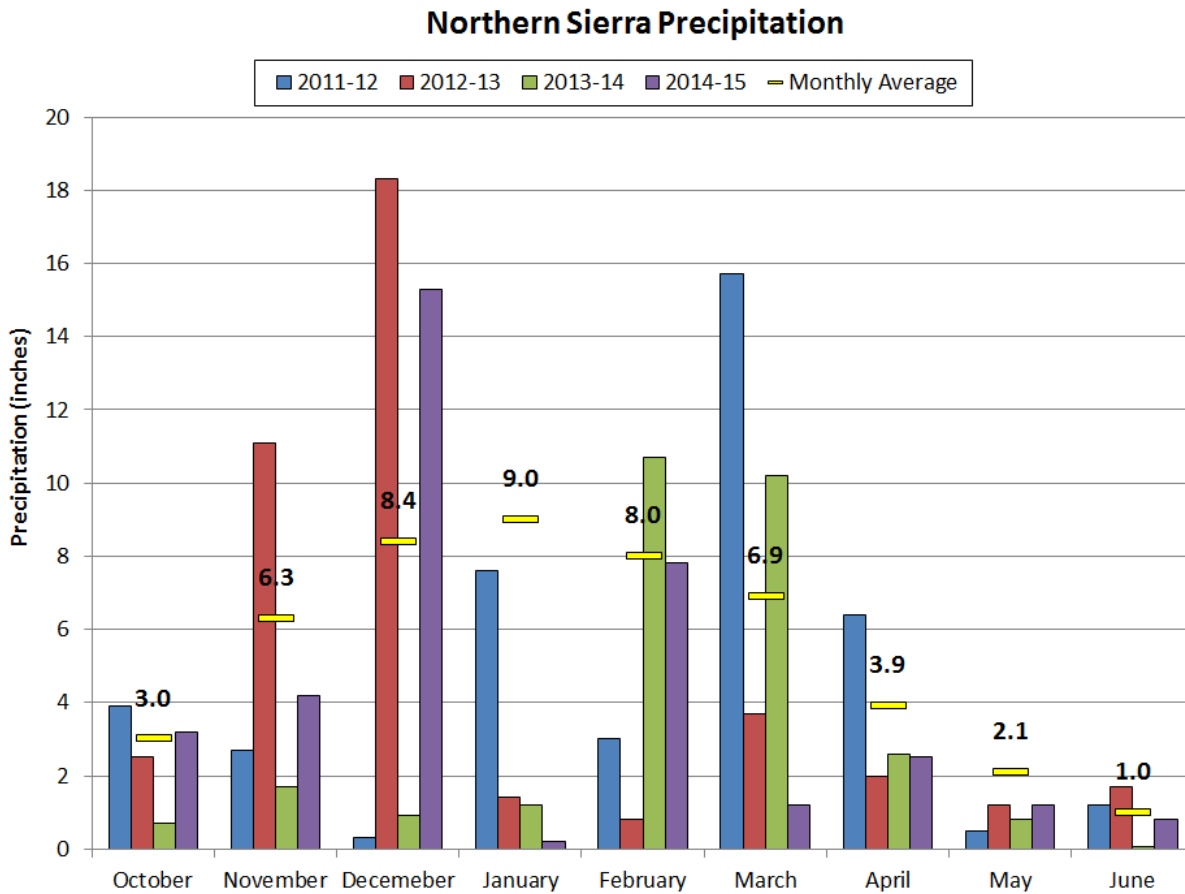
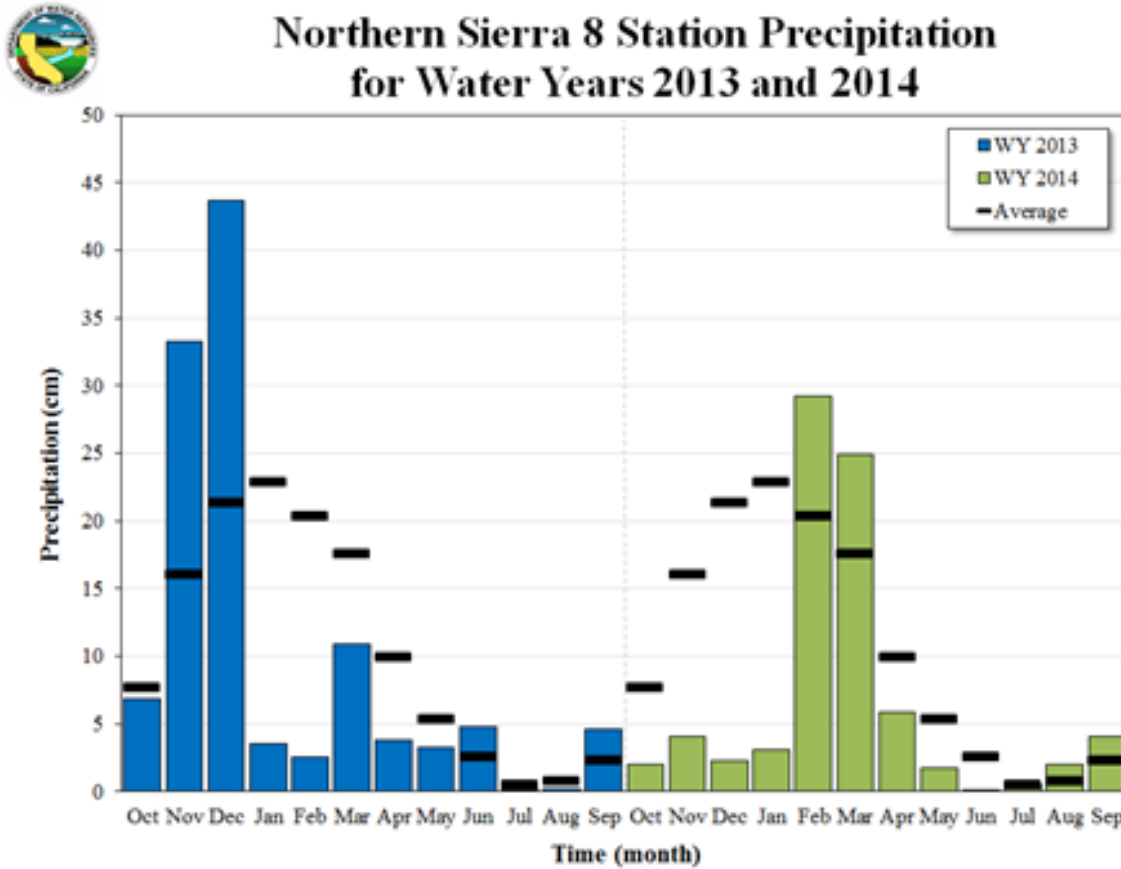


Figure 4. Northern Sierra Monthly Precipitation



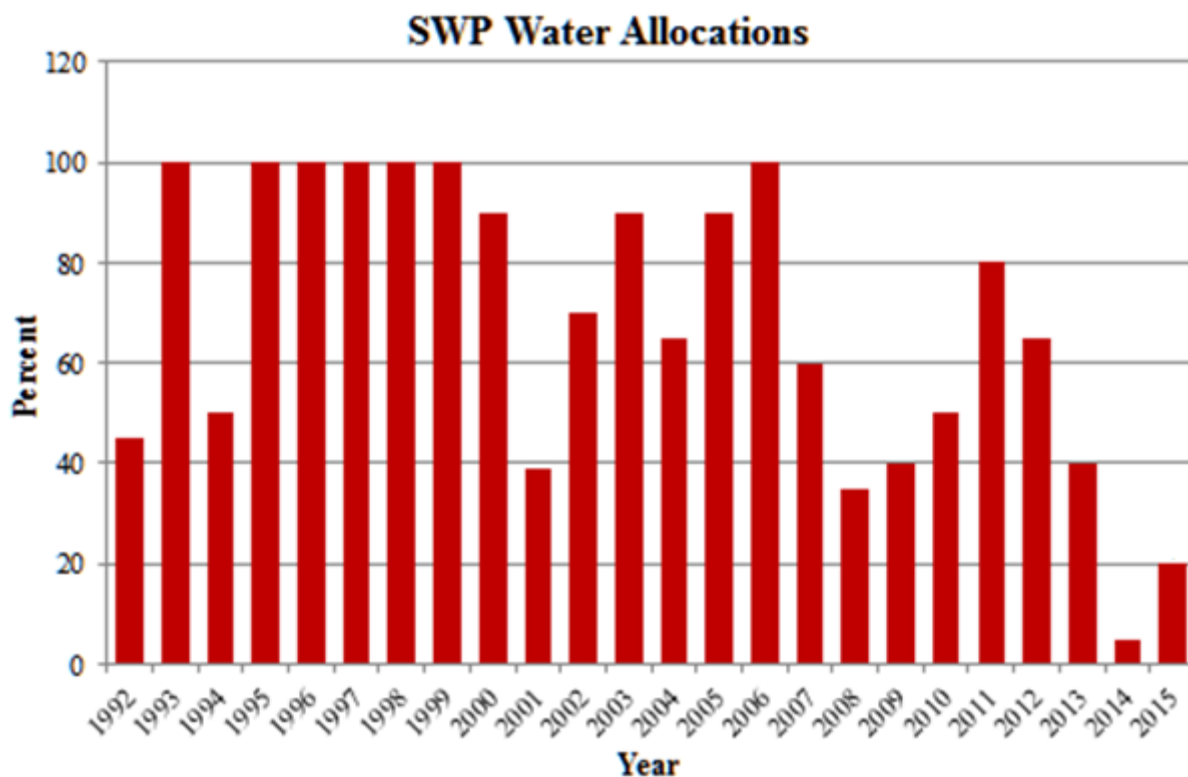
The extreme dryness continued into the next water year, with December and January, normally our wettest two months, being very dry at about 12 percent average. By January, 2014, with a bone dry winter thus far, a 10 percent snowpack, and with reservoir storage at 65 percent of average and 40 percent of capacity, we realized that California was heading for serious drought and the Governor declared on official drought on January 17. February produced one significant storm with some runoff and March was above average which gave some relief. But the April 1 snowpack was only 25 percent and drought resumed in April and continued into the following winter

The following winter, water year 2014-15, started hopefully. There was some rain in October and November and a wet December, 2014, with a couple good atmospheric river events, and about twice normal in the north. The southern Sierra did not fare as well with December a bit below average. There was virtually no rain in January which was very dry again, followed by one major warm storm in February. The wet season wound up with about 75 percent in the north and a bit under 50 percent in the southern half of the Sierra. The real surprise was the almost nonexistent snowpack with a record low 5 percent measured on April 1. That was due to lack of storms and much warmer temperatures during the few storms which did come.

Shortages during the last two years of drought were severe; the State Water Project delivered only 5 percent in 2014 and the federal Central Valley Project was not even able to supply the San Joaquin Valley Exchange Contractors, which reduced the Friant deliveries to near zero. Figure 5, SWP Water

Allocations, shows annual SWP delivery percentages. The State Water Project was able to garner a 20 percent supply out of the winter storm events, but the Central Valley Project saw a repeat of the dismal supply of 2014. For the second year in a row the meager flow of the San Joaquin River at Friant had to be sent downstream to the Exchange contractors, leaving little for the Friant Kern and Madera Canals.

Figure 5. Annual State Water Project Delivery Allocations



3. Water Supply

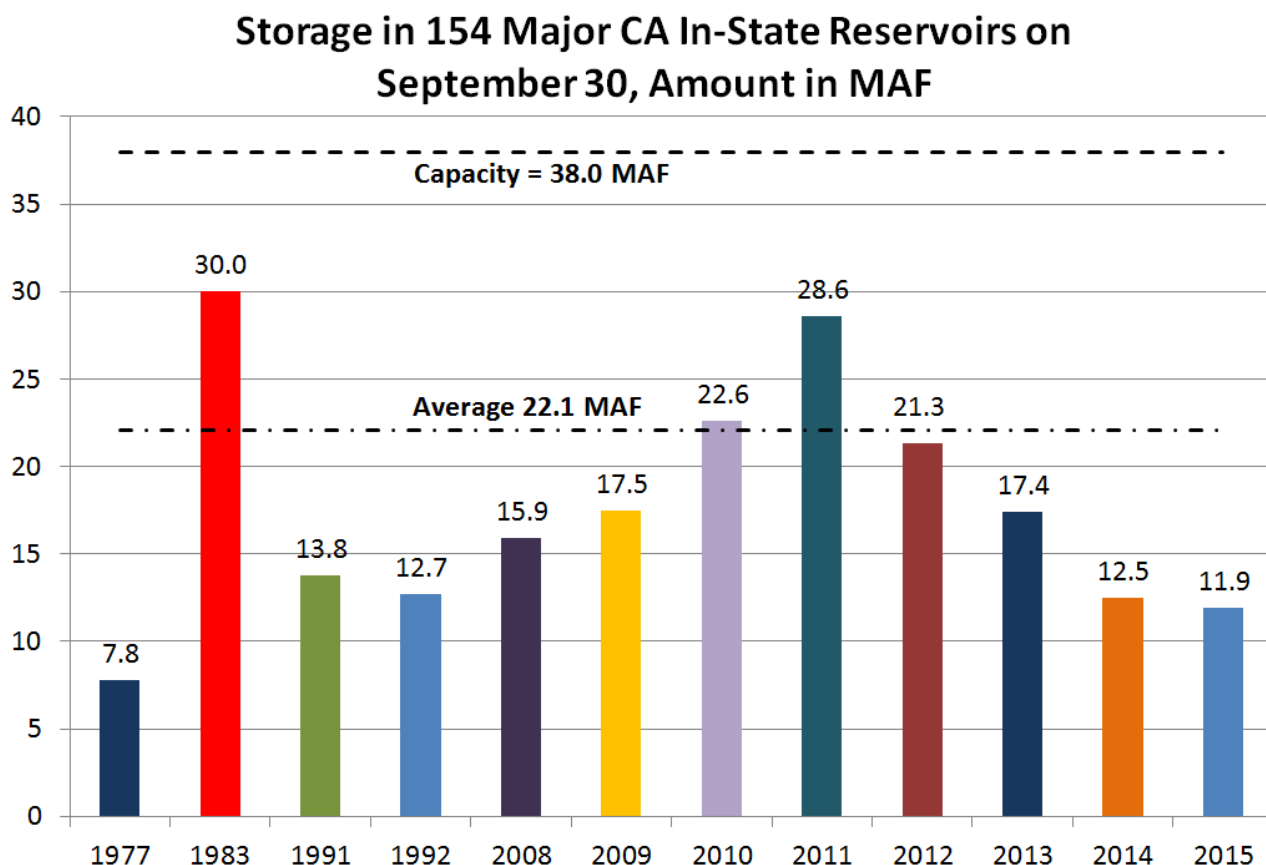
California has built many reservoirs to cushion drought severity; these work pretty well for a single year drought, but multiple years cause trouble. This time there were new fishery constraints, especially in the Sacramento-San Joaquin Delta export operations which decreased supplies further over that of past droughts, including loss of some of the federal Central Valley Project Exchange Contract water, which severely affected southern San Joaquin Valley water users.

Water year 2011 had been a good year with a good snowpack which generated about as much carryover storage as as one could ask—at 130 percent of average statewide water storage on September 30. Three years later, statewide storage had dropped to 12.5 million acre-feet¹, 57 percent of average and 33 percent of capacity (see Figure 6, Storage in 154 California In-state Reservoirs), a bit lower than the driest year of the 6 year 1987-92 drought, but more than the driest year in 1977 when only 7.8 million acre-feet, 36 percent of average, remained. Storage in this 2015 water year is tracking lower than a year ago. Beginning in early 2014, after the driest calendar year of record, new criteria for operation of the

¹ 1 acre-foot = 1,234 cubic meters and 1 acre = 0.405 hectare

Central Valley Project and the State Water Project with the limited supply available were developed with priorities for minimum urban health and safety (fire) needs, control of salinity intrusion from the ocean in the Delta and minimum protection of endangered species, including cold water for Sacramento River salmon. Some storms in December and February provided enough for a 20 percent delivery for the State Water Project in 2015, but comparably small amounts for CVP Delta exports, leaving major shortages in CVP supply for Project users south of the Delta again.

Figure 6. Water Storage in 154 Major California Reservoirs

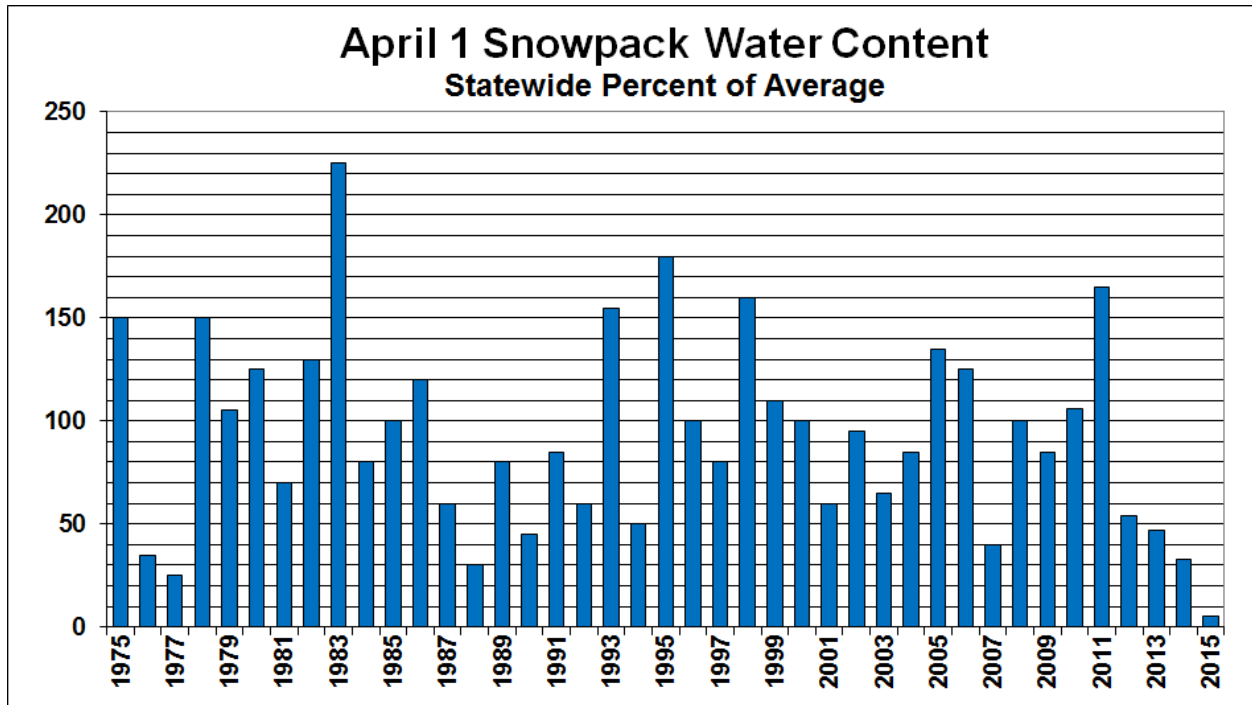


One of the notable factors in this 4 year drought is the warmer than average temperatures during the past two winters which impacts the portion of winter precipitation carried into the irrigation season by mountain snowpack. All four of the drought years had well below average snowpack ranging from about 50 percent in 2012 to only 5 in 2015. Figure 7 shows the history of April 1 snowpack water content for California. The previous low during 1977, our worst drought year, was 25 percent. But the winter storms of the last two years have been warmer than average with more rain than snow in the mountain watersheds. The measly 5 percent on April 1 of 2015 marks a new low and may presage what global warming would be like.

By the fall of water year 2015, estimated statewide water storage had fallen to about 11 million acre-feet, 29 per cent of capacity, but still above the historical low of about 7.5 million acre-feet in October 1977, our driest year. Part of the reason for higher levels was the strategy of keeping the CVP 4.5 million acre-feet Shasta Reservoir over 1 million acre-feet higher than the low of record in 1977 at the end of

summer 2015 to maintain enough cold water to preserve winter run salmon below the dam in the river. This reduced the amount which otherwise would have gone into San Joaquin Valley water supply.

Figure 7. April 1 California Snowpack



4. Impacts

There were about 9 million acres of irrigated land in California. In 2015, as estimated by the University of California, Davis (Howitt et al., 2015), about 540,000 acres were fallowed. The surface supply deficit, mostly in the Central Valley, was 8.7 million acre-feet. Additional ground water pumping (mostly from overdraft) of about 6 million acre-feet partly offset the deficit, leaving an agricultural deficit of 2.7 million acre-feet.

Urban water users were required to reduce 2015 water use by 25 percent with a range of 4 to 36 percent depending on past rates of water usage. Normal urban applied water use is about 9 million acre-feet statewide, although the net water use (depletion, which accounts for reuse) is more like 6 million acre-feet, which is about a quarter of the normal irrigated agriculture usage.

Another impact example is the effect on Pacific Flyway waterfowl. An estimated 4 to 6 million migratory birds winter in the Central Valley each year. Rice is an important crop in the northern Central Valley. According to the California Rice Commission, normally about 550,000 acres are grown. After harvest these farmers create about 300,000 acres of managed wetlands. In 2014, with 25 percent CVP water supply reductions, rice acreage was reduced to 435,000 acres and, in 2015, to 375,000 acres. After harvest, many of the rice lands are flooded and provide excellent food and forage for migrating waterfowl, vital for the Pacific flyway. Reduced acreage can lead to more crowding of birds with increased disease outbreaks. At one point it looked like only around 100,000 acres would have water for

flooding due to the shortages in 2015 water supply. Heroic efforts by farmers and the rice industry, with help from a wet December, were able to increase this to about 200,000 acres of flooded acreage this past winter season.

Fire is another aspect of drought. The drought and related moisture stress on forest trees allowed bark beetles to thrive. The combination of drought and beetles killed over 29 million trees in 2015, up from 3.3 million in 2014. And the bark beetle epidemic may be with us for a while. The 2015 wildfires burned an estimated 803,000 acres, starting in a big way in June and ending in November. With so many dead trees, fire danger will be high for several years. Total forest area in California is about 30 million acres, some 30 percent of the state's land area

5. Water Year 2016

What about the new water year? In 2016 there was an enormous difference in snowpack on April 1, about 85 percent this year compared to a record low of only 5 percent in 2015 (Figure 8). We were not sure what to expect after a dry February, but major storms in March (Figure 9) improved the water outlook greatly; 5 of the 6 major Sacramento region flood control reservoirs reached their storage limits and enough runoff occurred to put significant flows into the Yolo Bypass floodway. The northern third of the State recovered nicely, but amounts were less in the southern Sierra. With restrictions on CVP and SWP Delta export pumping, sizable shortages remain for the southern regions. Contrasted to the last two years, the CVP Friant Division will be delivering water this year to the upper valley. San Joaquin Valley local supplies are much less than demand even in normal years; long term solutions will require more water from the north.

Figure 8. 2016 Water Year Mid-Sierra Snowpack Buildup

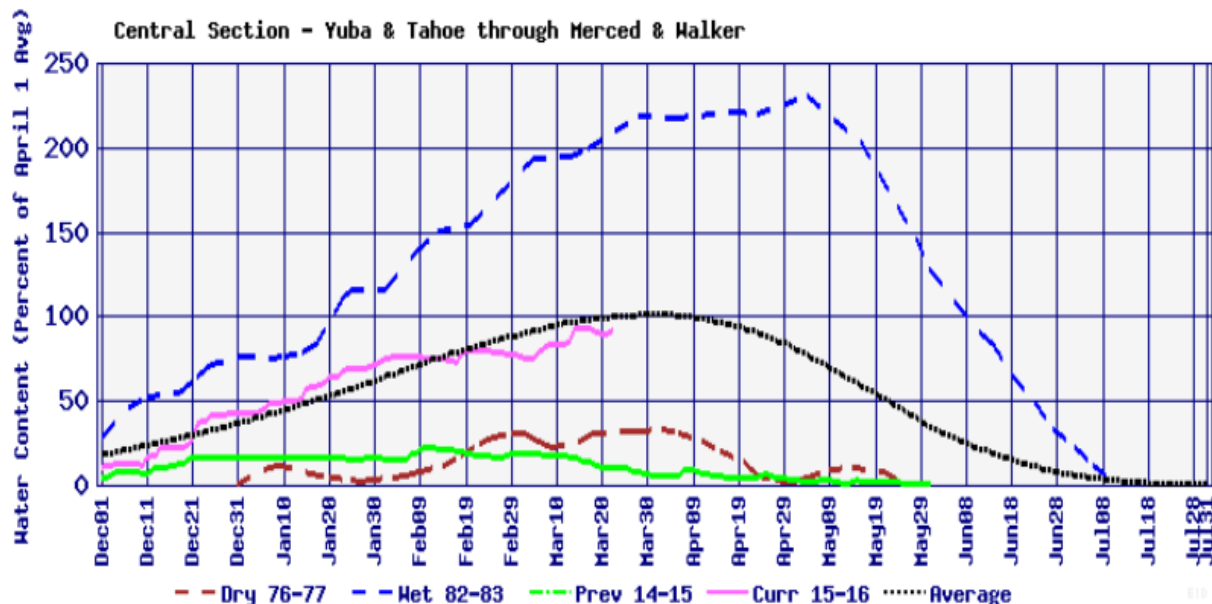
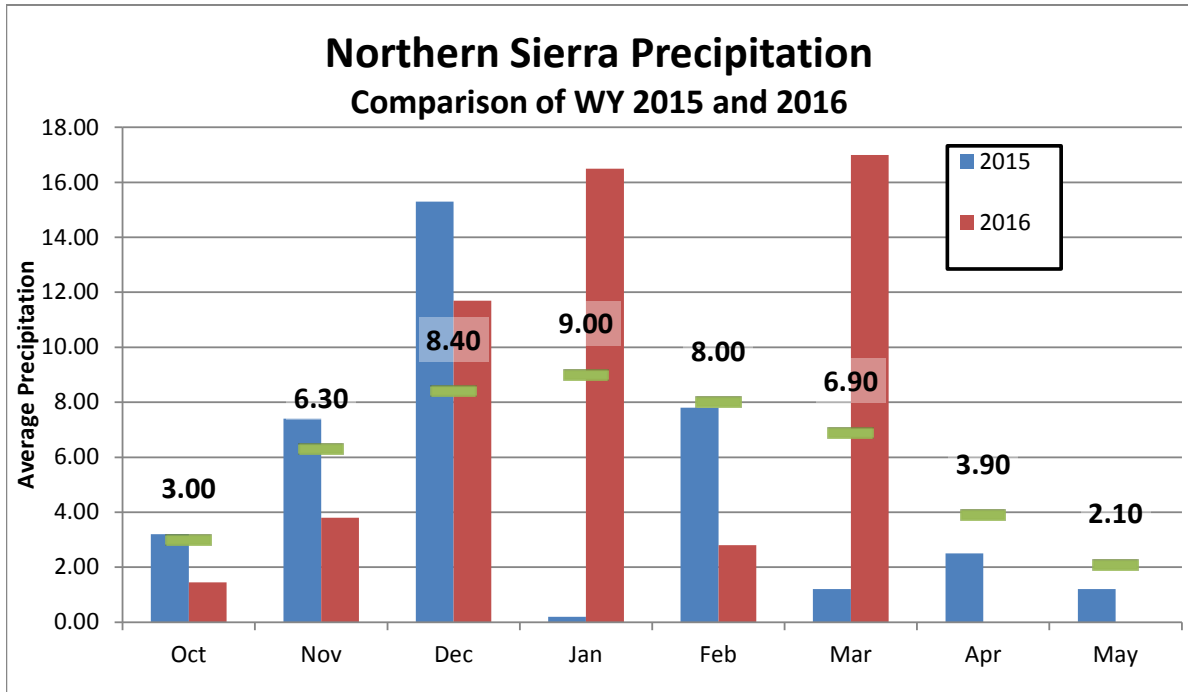


Figure 9. Northern Sierra Precipitation



6. References

Howitt, R., D. MacEwan, J. Medallin-Azuara, J. Lund, and D. Sumner (2015). *Economic Analysis of the 2015 Drought for California Agriculture*, UC Davis Center for Watershed Sciences, Davis, CA. Au

Hydroclimatic Characteristics of the 2012-2015 California Drought in a Historical Context

Minxue He¹, Mitchel Russo¹, and Michael Anderson¹

¹Division of Flood Management, California Department of Water Resources, 3310 El Camino Ave., Sacramento, CA. E-mail: kevin.he@water.ca.gov

Abstract

California experienced an extraordinary drought from 2012-2015 (which continues into 2016). The drought had both well perceived and more profound adverse impacts on the economy, society, and environment of the state. This work, from a hydrologic perspective, reviewed the development of this drought and examined its hydroclimatic characteristics at different temporal and spatial scales. Historical precipitation, temperature, snow water equivalent, full natural flow (observed and reconstructed), and reservoir storage data were collected and analyzed for this purpose. Results indicated that the 2012-2015 drought was unparalleled in 17 out of 26 indices investigated. The drought was caused by extremely low precipitation and record high temperature over the state. It was characterized by record low snowpack, exceptionally low April-July runoff, and below-average reservoir storage statewide. In general, the drought conditions in the South Coast, Central Coast, San Joaquin, and Tulare regions were more severe than other regions.

Keywords

California 2012-2015 drought; development; characteristics; historical context

1. Introduction

Drought is an economically and environmentally disruptive extreme event which can last from months to years. According to the Federal Emergency Management Agency (FEMA), drought causes an annual loss of \$6-8 billion on average over the United States. The specific impacts of drought vary from region to region depending on regional resilience and coping capacities. Advanced drought management practices are required to mitigate the adverse impacts of drought, which is particularly the case for dry areas including the State of California. Foremost of these practices is to understand the characteristics of drought events in a historical context.

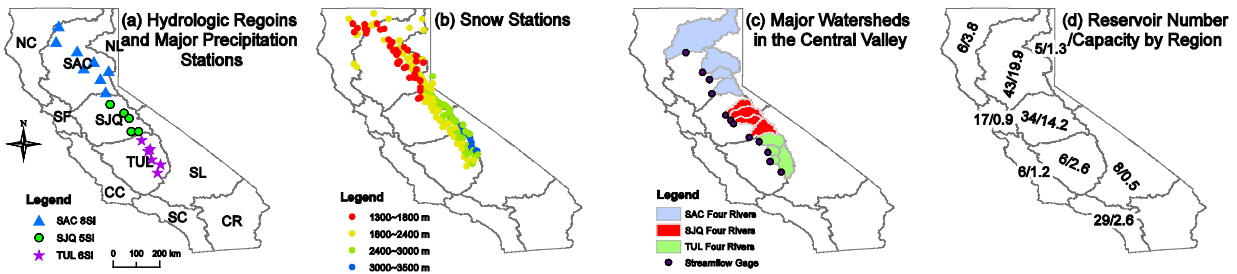
As a state with over 38 million people and a globally important economy, California is prone to drought with frequent drought events recorded. The most notable previous drought periods include 1929–1934, 1976–1977, 1987–1992, and 2007–2009. Currently the state is in a fifth year of another prolonged drought that originated in 2012. The first four years (2012-2015) of the drought stands as the driest and warmest four consecutive years in terms of statewide precipitation and temperature, respectively. The drought had both well perceived and more profound negative impacts on the economy, society, and environment of the state. For instance, record low water allocation (5%) for State Water Project contractors was registered in calendar year 2014. The objective of this study is twofold: 1) to investigate the development of the 2012-2015 California drought in a hydrologic framework; and 2) to assess its hydroclimatic characteristics at different temporal and spatial scales from an operational perspective. This information is critical for drought managers in making adaptive management plans.

The rest of the paper is organized as follows. Section 2 describes the study variables and metrics employed. Section 3 presents the results and findings. A short summary of the study is provided in Section 4.

2. Study Variables and Metrics

California Department of Water Resources (CDWR) maintains a network of precipitation, snow courses and pillows, and water level gages (for rivers and reservoirs) across the state along with a range of federal, local, and private agencies (Figure 1). CDWR divides the State into 10 major watershed drainage regions (Figure 1a). Of these 10 regions, three regions are of primary interest from a water supply's perspective: the Sacramento River Region (SAC), the San Joaquin River Region (SJQ), and Tulare Lake Region (TUL), since a major portion of the state's precipitation falls within these three regions and they provide much of the State's water supply. CDWR typically uses three primary precipitation indices, three river runoff indices, and two water supply indices in water planning and management practices. The precipitation indices include the Northern Sierra 8-Station Precipitation Index (8SI), San Joaquin 5-Station Precipitation Index (5SI), and Tulare Basin 6-Station Precipitation Index (6SI) (Figure 1a). The streamflow runoff indices include the SAC 4 River Index (SAC4), SJQ 4 River Index (SJQ4), and TUL 4 River Index (TUL4) (Figure 1c).

Figure 1. (a) Hydrologic regions and precipitation stations used in determining precipitation indices; (b) spatial distribution of 262 active snow courses; (c) major watersheds of the Central Valley; (d) number of reservoirs and the corresponding total capacity (in MAF) by hydrologic region.



This study focuses on aforementioned operational indices. Furthermore, the study analyzes the reconstructed annual full natural flow (Rec. FNF) for the SAC and SJQ regions. In addition, this study looks at statewide and regional precipitation, temperature, snow water equivalent, FNF, and reservoir storage (by the end of September (Res. Sept.) and May (Res. May) when reservoir stocks are normally at the minimum and maximum levels, respectively). The precipitation and temperature data are acquired from the National Centers for Environmental Information Climate Divisional Database (<http://www.ncdc.noaa.gov>). Other data are obtained from the California Data Exchange Center (CDEC, <http://www.cdec.water.ca.gov>). When investigating the temporal characteristics of the drought in a historical context, a total number of 26 variables are analyzed (Table 1). When determining the spatial characteristics of the drought, regional precipitation, temperature, AJ FNF, and reservoir storage (at the end of September) are analyzed since other variables are typically not available for all the hydrologic regions.

This study employs two metrics including the percent of average and historical rank in analyzing those variables. They are parsimonious metrics widely used in drought management and mitigation practices.

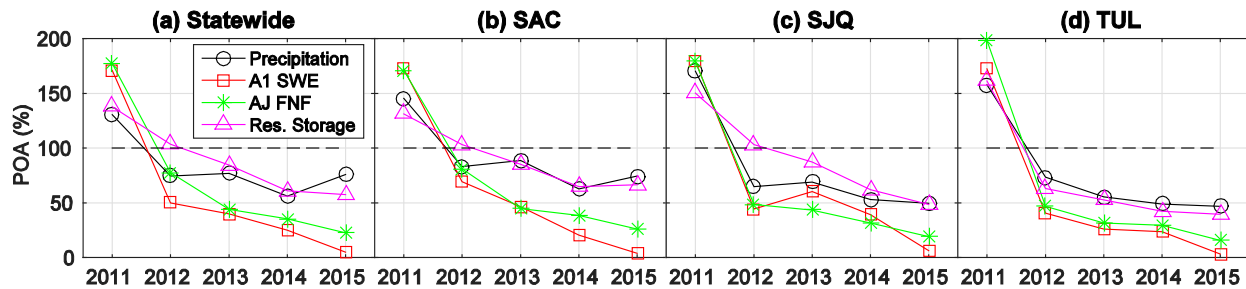
Table 1. Study variables and corresponding record period length

Statewide		SCA		SJQ		TUL	
Variable	Record Period	Variable	Record Period	Variable	Record Period	Variable	Record Period
Precipitation	1896-2015	8SI	1921-2015	5SI	1913-2015	6SI	1922-2015
Temperature	1896-2015	A1 SWE	1930-2015	A1 SWE	1930-2015	A1 SWE	1930-2015
A1 SWE	1950-2015	Annual FNF	1906-2015	Annual FNF	1901-2015	Annual FNF	1931-2015
Annual FNF	1941-2015	AJ FNF	1906-2015	AJ FNF	1901-2015	AJ FNF	1931-2015
AJ FNF	1941-2015	WSI	1906-2015	WSI	1901-2015	Res. (Sept.)	1976-2015
Res. (Sept.)	1976-2015	Rec. FNF	900-2015	Rec. FNF	900-2015		
Res. (May)	1976-2015	Res.(Sept.)	1976-2015	Res. (Sept.)	1976-2015		

3. Results and Discussion

Water year 2011 preceding the 2012-2015 drought has above average precipitation, A1 SWE, AJ FNF, and reservoir storage statewide and in the Central Valley (Figure 2). In contrast, water years 2012-2015 observe significantly below average precipitation, AJ SWE, and AJ FNF on the annual scale. Reservoir storages by the end of the water year 2012 (September 2012), however, are slightly above average statewide as well as for the SAC and SJQ regions. In general, an overall declining trend is evident in all four variables from 2011-2015 except for that statewide precipitation in 2015 is higher than each of its previous three years. Among four variables, A1 SWE has the largest deficiency followed by the AJ FNF. In 2015, the statewide A1 SWE (AJ FNF) is only 5% (23%) of average. Among three regions, the TUL region tends to be impacted the most with the lowest percent of average values in four variables in 2015. Overall, Figure 2 shows progressively increasing severity of the drought condition from 2012-2015.

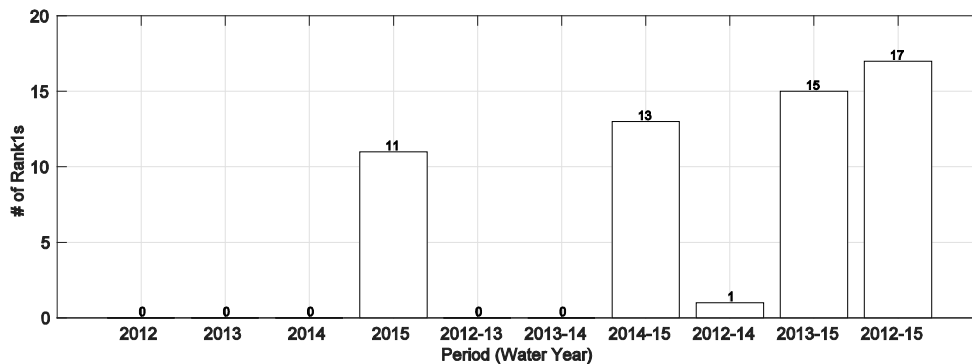
Figure 2: Percent of Average of (POA) of annual precipitation, A1 SWE, AJ FNF, and reservoir storage (September) from water year 2011-2015 for regions: (a) Statewide; (b) Sacramento (SCA); (c) San Joaquin (SJQ); (d) Tulare (TUL).



In addition to four variables investigated in Figure 2. Statewide annual average temperature from 2011-2015 is also compared to the long-term average. Year 2015 is the hottest year followed by 2014, with their annual average temperature higher than the long-term average by an amount of 4.0 °F and 3.1 °F, respectively. Water Years 2011, 2012, and 2013 also have higher than long-term average temperature, with a rate at 0.1 °F, 1.5 °F, and 2.0 °F, respectively. High temperature along with continuous deficiency in precipitation leads to significantly lower than average A1 SWE and thus exceptionally low AJ FNF. Shortfalls in precipitation, snowpack, and runoff contribute to below-average reservoir storage.

To obtain a general understanding on the severity of the drought at different temporal scales, 26 variables tabulated in Table 1 are ranked in their corresponding record periods according to their specific values at one- to four-year levels. For temperature, the highest value is ranked first, indicating the hottest condition. For other variables, the lowest value is ranked first, indicative of the driest condition. Either way, rank one indicates the most severe drought condition. Numbers of variables with rank ones within each (one- to four-year) sub-period from 2012-2015 are determined and illustrated in Figure 3. It is evident that at one-year level, no variables of 2012, 2013, or 2014 rank first in the record period. However, in 2015, 11 out of 26 variables rank first (either driest or hottest). At two-year level, 13 variables rank first in 2014-2015 (versus none in other two two-year sub-periods). Looking at three-year level, the sub-period 2013-2015 tends to be the drier one with 15 variables ranked first (versus 1 in 2012-2014). At four-year scale, 17 out of 26 variables rank first in their corresponding record periods. This indicates that, during 2012-2015, the driest single year is 2015; the driest two-year sub-period is 2014-2015; the driest three-year sub-period is 2013-2015. Additionally, Figure 3 also indicates the generally increasing tendency in drought severity from 2012-2015, as observed in Figure 2.

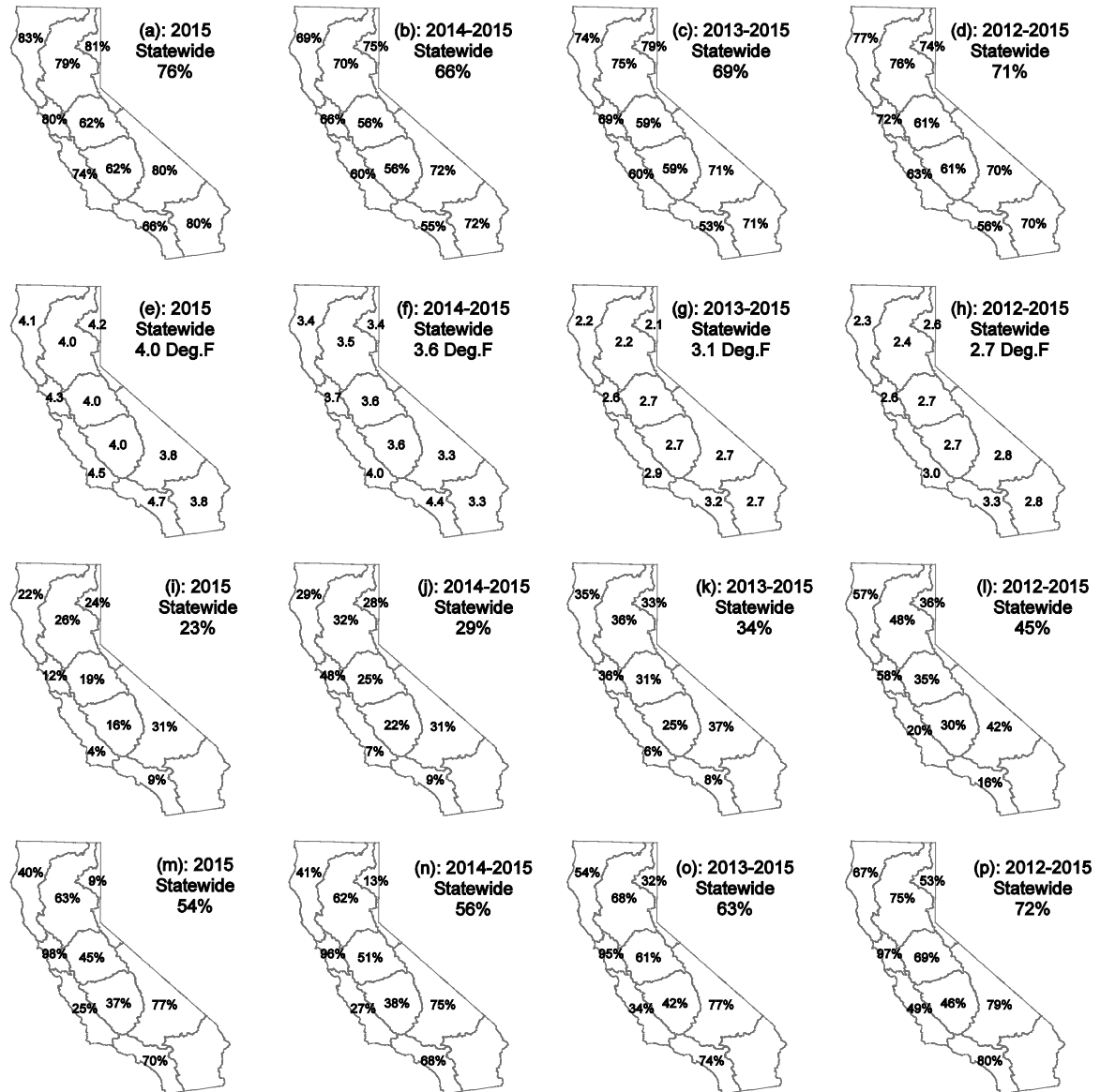
Figure 3. Number of variables (out of 26) ranked first within different periods from 2012-2015.



To investigate the spatial characteristics of the 2012-2015 drought, precipitation, temperature, AJ FNF, and reservoir storage (September) are compared to the average conditions at hydrologic regional scale in the driest one- to four-year sub-periods within 2012-2015 (Figure 4). For precipitation (first row of Figure 4), AJ FNF (third row), and reservoir storage (fourth row), the numbers highlighted in each region represent the percent of average (in %). For temperature (second row), the numbers denote the amount above average value for temperature (in Degree Fahrenheit). For precipitation, regions SJQ and TUL tend to have the lowest percent of average among all region at one-year level (2015). At two- to four-year level, the South Coast region tops the list, followed by regions SJQ/TUL. The Central Coast region has the third lowest percent of average at all four levels. For temperature, the South Coast region observes most significant increases in temperature at all four levels, followed by the Central Coast region. Looking at AJ FNF, the Central Coast region and the South Coast region still top the list. Specifically, at one- to three year levels, the Central Coast region sees the lowest AJ FNF; at four-year level, the South Coast region has the lowest AJ FNF. Regions TUL and SJQ rank after the Central Coast region and the South Coast region at two- to four-year levels. As for reservoir storage, the North Lahontan region tops the list (TUL region ranks third) at one- to three- year levels while the TUL region has the smallest percent of average (North Lahontan ranks third) at four-year level. The Central Coast region and the North Coast region rank second and fourth consistently at four levels. In addition to regional information, Figure 4 also shows the statewide conditions in different periods. It is evident that the percent of average of precipitation, AJ FNF, and reservoir storage at four-year level is generally the

highest. The above average temperature is also the lowest at four-year level. This indicates that when looking at a longer period, the drought conditions are relatively milder than which of a shorter period.

Figure 4. Precipitation (first row), temperature (second row), AJ FNF (third row), and September reservoir storage (fourth row) of the driest one- to four- year (first to fourth column, respectively) periods within 2012-2015 by hydrologic region.



4. Conclusions

This study shows that the 2012-2015 drought is caused by well below-average precipitation and record high temperature. The drought is characterized with record low April 1st snowpack, exceptionally low April-July runoff, and below-average reservoir storage. The periods 2015 and 2014-2015 tend to be the driest one-year and two-year sub-periods within 2012-2015, respectively. The period 2013-2015 is the

drier three-year sub-period within 2012-2015. The Central Coast, South Coast, San Joaquin, Tulare regions have the most severe drought conditions when looking at precipitation, temperature, and April-July runoff. When reservoir storage is used as the measure, however, the North Lahontan, Central Coast, Tulare, and North Coast regions have the most severe conditions.

Session 26. Multi-D Modeling

Flow Distribution of Confluence

(Fremont Weir, Sutter Bypass, Sacramento River and Yolo Bypass)

Sungho Lee / Ph D, PE/

CVFPB (Central Valley Flood Protection Board), DWR (Department of Water Resources)
3310 El Camino Avenue, Sacramento, California 95821, USA, Sungho.Lee@water.ca.gov

Abstract

The flow distribution/split near the Fremont Weir is studied and compared to 1997 and 2006 flood events using RMA 2 hydraulic model. Three cases of flood events (High Flow Discharge, Medium Flow Discharge and Low Flow Discharge) are simulated to study the discharge distribution and hydraulic parameters at the confluence of Sacramento River, Sutter Bypass, Yolo Bypass and Fremont Weir.

The simulation results comparing to the measured data are reasonably acceptable. They are matched with target values (measured stage data) at Fremont Weir and Verona for 1997 and 2006 flood events.

The water surface elevations (WSEL) and depth of East Fremont Weir are 1.04 ft and 0.74 ft lower than that of West Fremont Weir for the high and medium flood. For the low flood they remain almost same. The average velocities of East and West Fremont Weir are 6.51 ft/s and 3.78 ft/s for the high flood, 4.96 ft/s and 2.87 ft/s for the medium flood, and 3.79 ft/s and 3.99 ft/s for the low flood. The average velocity of East Fremont Weir is about 2.73 ft/s and 2.09 ft/s higher than that of West Fremont Weir for the high and medium flood. The average velocity of East Fremont Weir is about 0.2 ft/s lower than that of West Fremont Weir.

The flow distribution/split between the East and West Fremont Weir is 88% and 12% for the high and medium flood and 82% and 18% for the low flood. The more flow discharges flow to East Fremont Weir with high velocity and low WSEL for the high and medium flood.

Keywords

RMA 2D Model, East and West Fremont Weir, Sutter Bypass, Sacramento River, Yolo Bypass, Rattle Snake Island

1. Introduction

The Fremont Weir consists of East (Left) Fremont Weir, Rattle Snake Island and West (Right) Fremont Weir. The weir elevation of both Fremont Weirs is 30.50 ft (NGVD29).

RMA2 model is applied to study the hydraulic characteristics at the confluence of Sutter Bypass and Sacramento River near the Fremont Weir. Three cases (High Flow Discharge, Medium Flow Discharge and Low Flow Discharge) are simulated to calibrate related hydraulic parameters by this model.

Two inflows (Sacramento River near the Fremont Weir and Sutter Bypass) and three outflows (East Fremont Weir, West Fremont Weir and Sacramento River at Verona) are used for the boundary conditions.

Figure 1. Map of Fremont Weir (East and West) and Sacramento River



The input data for model simulation are obtained by the rating curve of the gauging stations of Fremont Weir (FRE) and Verona (VON) as follows:

Table 1. Input data for simulation Data

Event	Date	Fremont Weir (FRE)			Verona (VON)		
		RC		Measured	RC		Measured
		WSEL	Q	WSEL	WSEL	Q	WSEL
High Q	1/2/1997 23:00	39.47	397,000	39.47	39.09	104,000	39.09
Medium Q	1/2/2006 23:30	36.98	208,995	36.98	35.69	85,500	35.69
Low Q	4/6/2006 2:45	34.05	97,500	34.05	32.83	75,800	32.83

Q: Flow Discharge (cfs), RC: Rating Curve, WSEL: Water Surface Elevation (ft)

The inflow discharges for the Sacramento River and Sutter Bypass near the Fremont Weir are as follows:

Table 2. Inflow Discharges

Event	Total Q (cfs)	Inflow discharge (cfs)			
		Sacramento R. (Fr Weir)	%	Sutter Bypass and Feather R.	%
High Q	501,000	33,000	6.6	468,000	93.4
Medium Q	295,495	31,500	10.7	263,995	89.3
Low Q	173,300	27,000	15.6	146,300	84.4

Q: Flow Discharge (cfs), R.: River, Fr: Fremont

The material properties roughness, n coefficient, is used to consider the roughness of river bed, overbank and dense trees area in Sacramento River and Sutter Bypass. (refer Table 3)

Table 3. Material Property Roughness

Material Properties	Roughness, n value		
	High Flood	Medium Flood	Low Flood
Cultivated Field	0.03	0.03	0.03
Dense Trees	0.12	0.12	0.12
Grass	0.03	0.03	0.03
Main Channel	0.05	0.05	0.04
Main Channel 2	0.047	0.047	0.047
Mixed Channel Trees	0.048	0.048	0.048
Overbank	0.045	0.045	0.045
Scrub	0.09	0.09	0.09
Sparse Trees	0.08	0.08	0.08

2. Results and Discussion

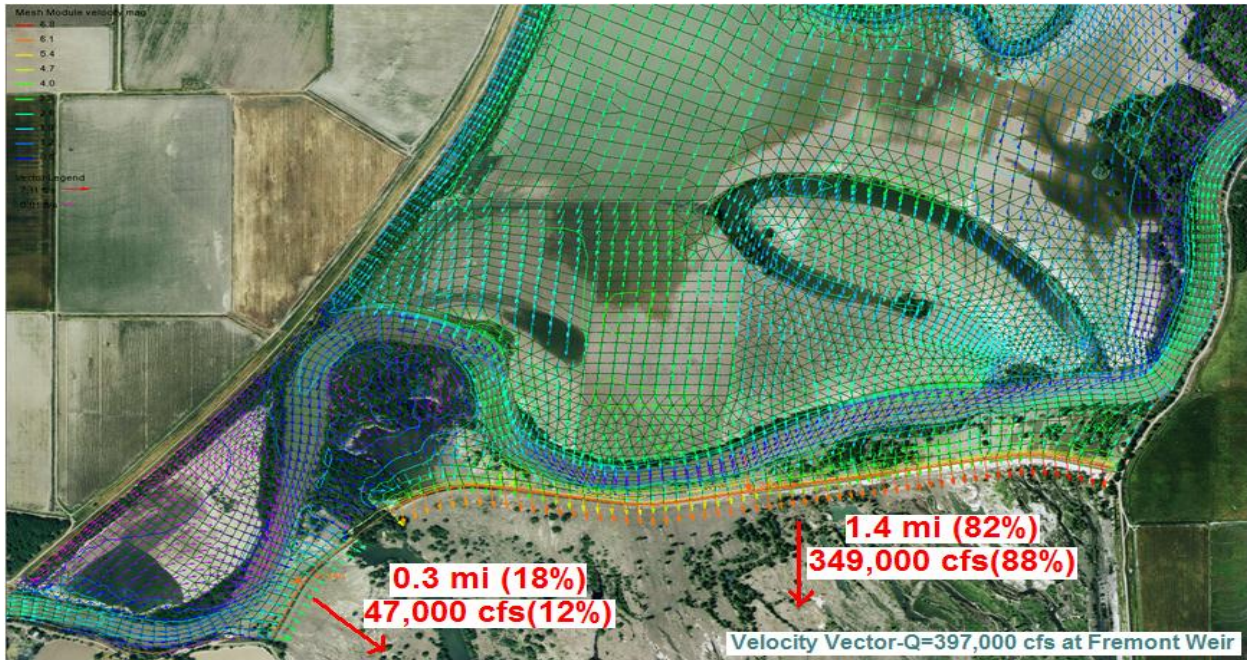
The simulation results are reasonable acceptable. They are matched with target values (measured stage data) at Fremont Weir and Verona. (refer Table 4)

Table 4. Simulation Result for Three Flood Events

Case	Date	Fremont Weir (FRE)				Verona (VON)			WSEL Diff
		Rating Curve		Simulation Result		Rating Curve		Measured	FRE-VON
		WSEL	Q	WSEL	Diff	WSEL	Q	WSEL	ft
High Q	1/2/1997	39.47	397,000	39.48	+0.01	39.09	104,000	39.09	+0.38
Medium Q	1/2/2006	36.98	208,995	36.73	-0.25	35.69	85,500	35.69	+1.29
Low Q	4/6/2006	34.05	97,500	34.12	+0.07	32.83	75,800	32.83	+1.22

Q: Flow Discharge (cfs), RC: Rating Curve, WSEL: Water Surface Elevation (ft), Diff: difference

Figure 2. Velocity Vectors for High Flood



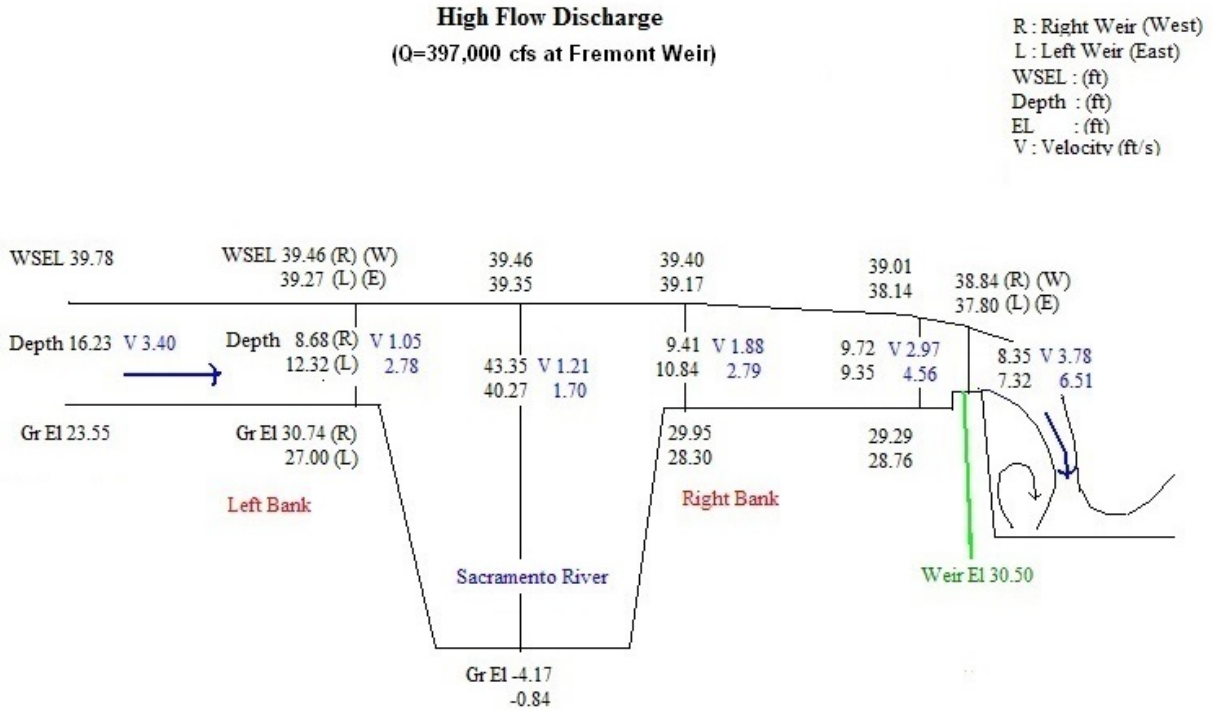
Hydraulic characteristics near the Fremont Weir are summarized in the following table.

Table 5. Simulation Result near the Fremont Weir

	Location	West Fremont Weir				East Fremont Weir			
		Gr El	H	V	WSEL	Gr El	H	V	WSEL
High Q	North Bank	30.74	8.68	1.05	39.46	27.00	12.32	2.78	39.27
	Sac River	-4.17	43.35	1.21	39.46	-0.84	40.27	1.70	39.35
	South Bank	29.95	9.41	1.88	39.40	28.30	10.84	2.79	39.17
	Up of Weir	29.29	9.72	2.97	39.01	28.76	9.35	4.56	38.14
	Fr Weir	30.50	8.35	3.78	38.84	30.50	7.32	6.51	37.80
Medium Q	North Bank	30.74	5.95	0.66	36.70	26.97	9.56	1.65	36.51
	Sac River	-4.17	40.73	1.39	36.71	-0.84	37.47	1.10	36.53
	South Bank	29.95	6.62	1.36	36.68	28.30	11.92	1.75	36.43
	Up of Weir	29.29	7.16	2.11	36.41	28.76	6.99	3.12	35.78
	Fr Weir	30.50	5.81	2.87	36.29	30.50	5.07	4.96	35.55
Low Q	North Bank	30.74	3.35	0.33	34.07	26.97	6.96	0.83	33.96
	Sac River	-4.17	37.98	2.13	34.08	-0.84	34.99	0.99	33.96
	South Bank	29.95	4.21	1.21	34.05	28.30	5.90	0.99	33.91
	Up of Weir	29.29	4.29	2.18	33.58	28.76	4.80	1.90	33.54
	Fr Weir	30.50	2.86	3.99	33.33	30.50	2.92	3.79	33.39

Q: flow discharge (cfs), Fr: Fremont, Up: upper, Sac: Sacramento, Gr El: Ground Elevation, H: depth (ft), V: velocity (ft/s), WSEL: Water Surface Elevation (ft)

Figure 3. WSEL, Depth and Velocity for High Flood (Q=397,000 cfs)



The WSEL and depth of East Fremont Weir are 1.04 ft and 0.74 ft lower than that of West Fremont Weir for the high and medium flood. For the low flood they remain almost same. The average velocities of East and West Fremont Weir are 6.51 ft/s and 3.78 ft/s for the high flood, 4.96 ft/s and 2.87 ft/s for the medium flood, and 3.79 ft/s and 3.99 ft/s for the low flood. The average velocity of East Fremont Weir is about 2.73 ft/s and 2.09 ft/s higher than that of West Fremont Weir for the high and medium flood. The average velocity of East Fremont Weir is about 0.2 ft/s lower than that of West Fremont Weir.

The outflow discharges and discharge distribution at Fremont Weir are as follows:

Table 6. Outflow Discharges and Discharge Distribution at Fremont Weir

Event	Total Discharge (cfs)	Outflow						
		Sutter Bypass				Sacramento River		
		(Fremont Weir)		Detailed	Total	(Verona)		Total
WSEL (ft)	Q (cfs)	%	%	WSEL (ft)	Q (cfs)	%		
High Q	501,000	39.47	397,000	100	79.2	39.09	104,000	20.8
West Fr. Weir			47,640	12.0	9.5			
East Fr. Weir			349,360	88.0	69.7			
Medium Q	294,495	36.98	208,995	100	71.0	35.69	85,500	29.0
West Fr. Weir			25,080	12.0	8.5			
East Fr. Weir			183,915	88.0	62.5			
Low Q	173,300	34.05	97,500	100	56.3	32.83	75,800	43.7
West Fr. Weir			17,060	17.5	9.8			
East Fr. Weir			80,440	82.5	46.4			

Q: Flow Discharge (cfs), Fr: Fremont Weir, WSEL: Water Surface Elevation

3. Conclusions

The flow distribution/split between the East and West Fremont Weir is 88 % and 12 % for the high and medium flood and 82 % and 18 % for the low flood. The more flood discharges flow to East Fremont Weir with high velocity and low WSEL for the high and medium flood events.

The flow distribution/split between Sutter Bypass (including Feather River) and Sacramento River (Verona) is 79 % and 21 % for the high flood and 71 % and 29 % for the medium flood, and 56 % and 44 % for the low flood. The more flood discharges flow from Sutter Bypass to Yolo Bypass through the Fremont Weir during the flood events. The main stream of Sutter Bypass flows to the East Fremont Weir directly and the West Fremont Weir acts as a secondary weir for all three flood events.

Flow distribution/split at the East and West Fremont Weir should be studied by 2 or 3-dimensional model for further projects of long term flood management, channel capacity, setback levee, fish ladder and existing weir extension. One dimensional model is not enough to represent hydraulic phenomenon for the complex confluence near the Fremont Weir.

4. References

SMS Tutorials Version 10.0, August 24, 2011, Aquaveo

Users guide to RMA2 WES Version 4.5, US Army, Engineer Research and Development Center

Users guide to GFGEN – Version 4.27, US Army Corps of Engineers